Micro/nano liquid ejection via electrohydrodynamic fields and gaseous streams. Application in structural biology with XFEL

FRANCISCO CRUZ MAZO

PhD Thesis

2019

UNIVERSIDAD Ð SEVILLA

Micro/nano liquid ejection via electrohydrodynamic fields and gaseous streams. Application in structural biology with XFEL.

A dissertation submitted by

Francisco Cruz Mazo

to Department of Aerospace Engineering and Fluid Mechanics

in partial fulfilment of the requirements for the degree

Doctor of Philosophy

in the subject of Fluid Mechanics

Advisor: Prof. Dr. Alfonso M. Gañán Calvo

Co-advisor: Prof. Dr. José M. Montanero

A mis padres

Acknowledgments

Los medios deben ser
homogéneos con el fin.

Antonio García-Trevijano

The measure of a man is
what he does with power.

Pláton

It is not living that matters,
but living rightly.

Sócrates

I would like to thank the advisor and co-advisor of this Ph. D. thesis, Alfonso M. Gañán-Calvo and José M. Montanero, respectively, for giving me the opportunity and support to research on this exciting field of study. Particularly, I want to emphasize my gratitude to Alfonso for all his trust and encouragement. The combination between his scientific rigor and his ability to transfer knowledge through applications makes him a real reference for young investigators like me. In addition to all I could learn from him, it must be also recognized to him how his wisdom method of guidance allows one not only to keep the focus on fundamentals and objectives, but also to gain both independence and maturity. So, I was fortunate to enjoy that kind of balance between supervision and freedom. Thank you very much for your past and future teachings, my master.

My especial gratitude also goes to Henry N. Chapman and his group for their warm reception and hospitality during my five-months stay at the Center for Free-Electron Laser Science, DESY (Germany).

Institutionally, my acknowledgment goes to the state of España for the Ph. D. fellowship received. Also to the Ph. D. Programme Ingeniería Mecánica y Organización Industrial of Universidad de Sevilla. Of course, to the Department Ingeniería Aeroespacial y Mecánica de Fluidos for the good work environment and particularly to my office colleagues for some remarkable moments: Alonso, Bea, Eulalia, Gusti, Julio y Sergio.

Additionally, I want to recognize at this point the relevant role that some teachers and professors somehow played along my path as student from Elementary School to this moment, particularly: José Causse, Manuel Ortega, Práxedes Caballero, Antonio R. Yaque, Manuel Toscano, Heliodoro González, Miguel Pérez-Saborid and Miguel A. Herrada.

Lastly, my gratitude to Maria Luiza, my girlfriend and future wife, for all her love, patience, empathy and wise advices. To my sisters, Gema y Estrella, because their experiences on a similar road were an asset for me. I am especially grateful to my parents, Paco y Estrella, for all their unconditional love, support, advices and the way they educated me under solid moral values so necessary in both science and life: *honor*, *dignity* and *humbleness*. Padres, esta tesis es para vosotros.

In Sevilla, th 2019

Paco

Contents

List of Figures

Chapter 1

Introduction

> The last thing one discovers
> in composing a work is
> what to put first
>
> Blaise Pascal

This first chapter will provide the reader an overview regarding the topic of this work, its motivation and how it is organized in the following chapters. Specifically, we will focus on the state-of-the-art of jets and droplets produced by capillary cone-jet configurations. Then, we will state the main challenges in terms of sample delivery for structural biology analysis with XFEL and particularly for experiments in Serial Femtosecond Crystallography.

1.1 On the approaches to Fluid Mechanics

The scientific discipline of Fluid Mechanics is devoted to studying how fluids behave under the action of forces. Since 1822, the general theoretical framework is formed by the well-known Navier-Stokes equations. We can read its generic version for compressible fluids,

$$\frac{\partial \rho_f}{\partial t} = -\nabla \cdot \left(\rho_f \boldsymbol{v_f}\right) \tag{1.1}$$

$$\rho_f \frac{D\boldsymbol{v_f}}{Dt} = \nabla \cdot \bar{\bar{\tau}} + \rho_f \boldsymbol{f_m} \tag{1.2}$$

$$\rho_f \frac{D\left(e + v_f^2/2\right)}{Dt} = \nabla \cdot \left(\bar{\bar{\tau}} \cdot \boldsymbol{v_f}\right) + \rho_f \boldsymbol{f_m} \cdot \boldsymbol{v_f} - \nabla \cdot \boldsymbol{q} + Q_r + Q_q \tag{1.3}$$

where, $\bar{\bar{\tau}} = -\nabla p + \bar{\bar{\tau}}'$ are the normal and shear stresses on a infinitesimal volume of fluid exerted by the pressure gradient ∇p and the viscous forces $\bar{\bar{\tau}}'$ that are balanced to the substantial derivative of momemtum $\rho_f D\boldsymbol{v_f}/Dt = \partial \boldsymbol{f_m}/\partial t$ and the mass forces $\boldsymbol{f_m}$. These equations are valid if the fluid domain is assumed to be a continuum medium. In other words, the characteristic length L_f of the fluid must be larger than the characteristic length $(\delta\Omega)^{1/3}$ (i.e., $\delta\Omega$ is the minimum volume required for an accurate collection of a certain physical measurement). Consequently, that minimum volume $\delta\Omega$ should be much larger than the averaged molecular distance d_m: $d_m \ll (\delta\Omega)^{1/3} \ll L_f$.

The intrinsic complexity of the previous equations makes it hard to find analytical solutions out of academic problems. So, alternative approaches have been explored in the literature as strategies of resolution based on analogy and similarity to capture the physics of fluid flow.

Dimensional analysis has been historically linked to this discipline, allowing us to find what parameters affect the features of a flow. For instance, a remarkable case is one of the problems studied by Sir G. I. Taylor (1950a, 1950b). He was able to find the functional dependence of the shock wave radius r_f produced in the first artificial nuclear explosion ever (called as the *Trinity test*). To do so, the chosen parameters were the energy E concentrated in the initial radius, the density of the ambient air ρ_o and the time reckoned from the moment of explosion t. So, we can easily assume the functional relation $r_f = f(E,t,\rho_o)$, which can be made dimensionless by using the Π-Buckingham Theorem. So, $r_f \cdot \left(Et^2/\rho_o\right)^{-1/5} = C(\gamma)$, where C is a fixed coefficient for a certain value of the adiabatic index γ. The latter expression matches excellently with the experimental evolution of the radius (see Fig. 1.1).

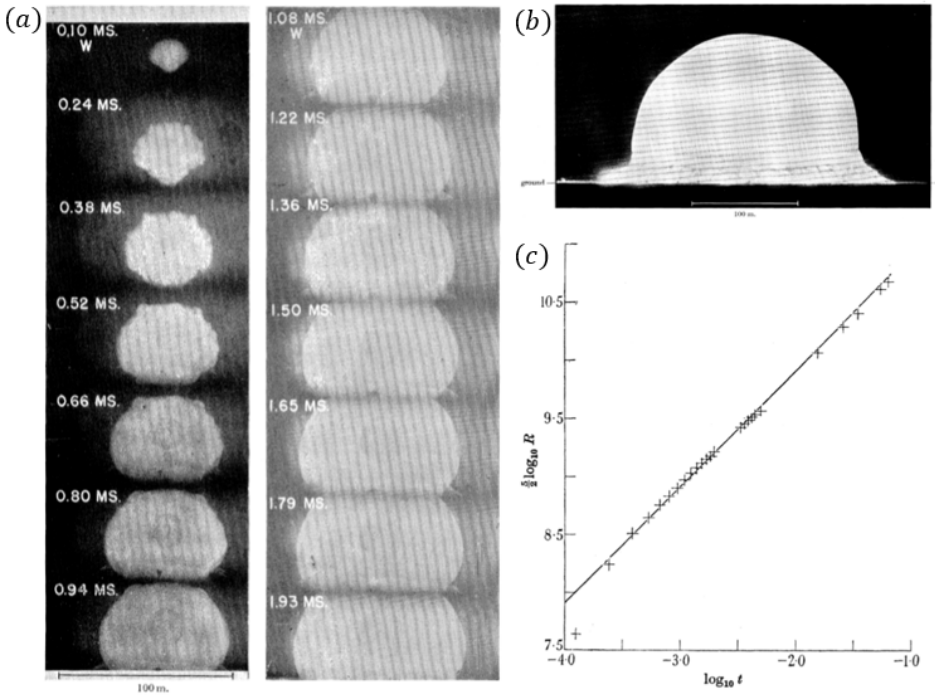

Figure 1.1: Trinity test (a) Sequence of images of the explosion with an interval of 0.14 ms (b) Snapshot at 15 ms after the explosion begins (c) Scaling law (solid line) and experimental points (crossed marks). (a), (b), (c) Republished figures with permission of Royal Society of London, from (G. I. Taylor, 1950a); permission conveyed through Copyright Clearance Center, Inc.

These first-order models do help very much not only for understanding the underlying physical mechanisms behind a specific phenomenon, but also for providing a very useful insight so that practitioners can control and optimize their processes in applications. In this thesis, we will use this kind of dimensionless analysis. So, we will take advance of the great power of scaling arguments for deriving physical laws.

Stability analysis - One of the most complex problems in fluid mechanics concerns to the study of liquid entities in the absence of rigid walls. This leads to the additional unknown of the interface location. In particular, jets are characterized by a longitudinal spatial coordinate whose typical length L_z is much larger than any characteristic radial length within

the fluid domain L_x, L_y. Tracking the jet interface is a matter of an extensive study because can entail the appearance of singularities in the fluid domain. For instance, our daily experience teaches us that an emerging jet from a tap breaks into droplets at a certain distance downstream or alternatively, we can observe how a honey-jet suffers whipping movements when is diving our cup of tea. Although closed dimensionless descriptions hardly approach this kind of instabilities, the role of classical numbers with unity dimension is significant to classify flows according to scales. Indeed, they are useful to provide threshold values for asymptotic analyses. In this regard, some of the most relevant numbers for our purposes are included in the following table.

Number	$\text{Term}_1/\text{Term}_2$	Expression
Weber	$\frac{kinetic\ energy}{surface\ tension}$	$We = \frac{\rho_f v_f^2 L}{\sigma}$
Reynolds	$\frac{inertia}{viscous\ forces}$	$Re = \frac{\rho_f v_f L}{\mu_f}$
Ohnesorge	$\frac{viscous\ forces}{(inertia \times surface\ tension)^{1/2}}$	$Oh = \frac{\mu_f}{\left(\rho_f \sigma L\right)^{1/2}}$
Bond	$\frac{gravity}{surface\ tension}$	$Bo = \frac{\rho_f g L}{\sigma}$
Froude	$\frac{inertia}{gravity}$	$Fr = \frac{v_f}{(gL)^{1/2}}$

Within this exciting world of liquid ejecta, we are particularly interested in those at the micro and nanoscale. This is typically linked to neglecting gravity forces against with surface tension, inertia and viscous sinks ($Fr \gg 1$, $Bo \ll 1$). For this type of jets, a classical approach is the use of stability analysis for the prediction of those singular points in the fluid domain.

Stability theories have been and remain a topic of great interest for the fluid mechanics community, accumulating and investing many efforts. Here, we will give a brief picture of how their ways have suffered many changes along the last decades. Stability of solutions entails the consideration of a candidate steady-state base flow to be evaluated. In general, a certain solution $U(x,t)$ can be composed as the sum of two terms, the steady-state $U_o(x)$ and a transient term that oscillates around the latter one $\eta \cdot U_p(x,t)$, where η is a parameter. If we impose that U_p is small enough, then $\eta \ll 1$. So, we are under proper conditions to linearize the governing equations around the steady state for a description of the flow stability. Note that it is inherently assumed that there is not an energetic transfer between modes. Thus, we can realize a normal decomposition

of modes Ψ_i for a linear response of the system under perturbations. If we assume a separation between spatial and temporal dependence such as $U_p(x,t) = \sum_i^N (\Psi_i(x) \cdot e^{\omega_i t})$, the problem is reduced to the calculation of N spatial modes Ψ_i that are purely shown at their respective frequencies ω_i. For ensuring the asymptotic attenuation of U_p towards the base flow, all ω_i must be negative. So, we could say that the system is asymptotically stable. On the other hand, if it existed any $\omega_i > 0$, the corresponding mode Ψ_i would be amplified *ad infinitum* at the computed growth rate. So, we could say that the system diverges from the basic flow. Strictly speaking, experimental situations may show that the latter condition turns out necessary but not sufficient for the flow instability, since the effect of non-normal mode composition and nonlinear effects could eventually damp the unstable mode when reaches a certain finite amplitude. It must also be remarked that a linear stability analysis assumes an infinitesimal amplitude of the perturbations involved.

Local vs Global analysis - Despite the mentioned limitations, this type of approaches has been extensively used in the literature for predicting bifurcations or singularities in flows with a good degree of matching. Classically, linear stability analyses have been performed together with strong assumptions regarding the fluid domain and boundary conditions. In this regard, unbounded liquid columns are assumed for temporal analysis, so as semi-infinite liquid cylinders are fluid domain used in spatial analyses. A combination is the spatio-temporal analysis, which leads to more accurate results for free-surface flows fed from tubes. For the latter type of analysis, we can distinguish two main instability mechanisms: the convective one, where the perturbation is transported downstream and eventually would provoke the breakup of the jet; and the absolute instability, which is typically linked to dripping (see Fig. 1.2) and where the information is able to travel from downstream to upstream. However, these local analyses do not successfully capture the dripping-jetting transition for highly-stretched liquid flows such as cone-jet configurations. Indeed, this challenge demands to take into account the boundary conditions of the problem for a global stability approach. This will be studied in the Chapters 3 and 4.

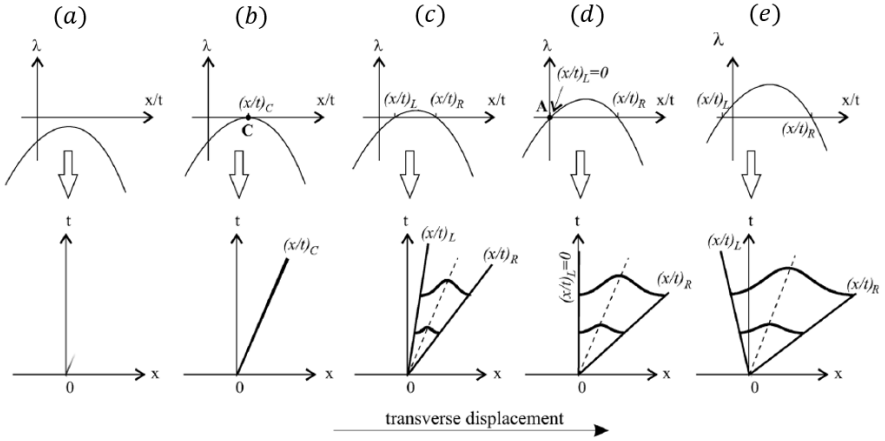

Figure 1.2: Schematic diagram of the convective and absolute instability for an initial perturbation placed at the origin in a 1D configuration: (a) stable, (b) marginal convective instability, (c) convective instability, (d) marginal absolute instability, (e) absolute instability. Reprinted with permission from (G. Agez et al., 2007). Copyright (2007) by the American Physical Society.

1.2 Fluid fragmentation: jets and drops

Perhaps, the most straightforward way of producing liquid ejecta is just pushing a liquid with a pressure difference large enough through a tube. However, if the tube diameter decreases, surface tension forces exert a stronger resistance over the flow dynamics (i.e., $Fr \sim 1$ and $Bo \sim 1$). This inherently entails an increase of the driving pressure required ΔP. Besides, if one is interested in micron-sized liquid jets and drops, tubes with similar diameters lead to many problems such as clogging issues, loosing of robustness in operation, bad reproducibility, etc. So, ideally, we would like to extract in a controllable way a certain liquid flow rate Q_ℓ from an attached meniscus to a tube tip. The purpose is to form a slender liquid ejection from a much bigger feeding tube (see Fig. 1.3). For example, *Electrospray*, where we can use distance pulling forces by imposing high electrical fields onto the hydrodynamic domain. In contrast, the use of an additional active wrapping fluid phase plus geometry can change the shape of the meniscus to a cone. The latter concept is well-known as *Flow Fo-*

cusing. So, produced by either electrohydrodynamic fields or by mechanical means, cone-jet methods have enabled the increase the stretch ratio of the flow, allowing the generation of small fluid entities as liquid jets and drops within gas streams or vacuum as well (Zeleny, 1914), (Gañán-Calvo, 1998), (Loscertales et al., 2002), (Gañán-Calvo, 2005), (Gañán-Calvo et al., 2007) (see Fig. 1.4). Note that these configurations also allow one to produce liquid drops within host liquids (Anna et al., 2003), (Cohen et al., 2001), (Utada et al., 2005), so as the delivery of microbubbles in liquid streams (Gañán-Calvo & Gordillo, 2001) (see Fig. 1.5). The beginning of this story started when Zeleny (1914, 1917) reported the first experiments on the effect of electric fields on a liquid meniscus and how its shape changes to a characteristic conical form. Then and a fine aerosol is ejected downstream from the jet breakup and charge repulsion. Passed the middle of 20th century, the phenomenon was brought to light again by Vonnegut and Neubauer (1952) and a few years later G. Taylor (1964) found the first theoretical explanation for the stability of electrified conical shapes, since then called *Taylor cone*. Essentially, Taylor assumed a perfect conductor liquid and a pressure difference ΔP_s across its interface owing the well-known Debye layer. So, there exists a jump for the normal electrical field E_n between the liquid bulk and the outer domain. Gauss's equation evaluated onto a differential volume $\delta\gamma$ provides an estimation for the surface charge as $\sigma_e = \varepsilon_o E_n - \varepsilon E_{ni} \approx \varepsilon_o E_n$. For a strong enough voltage difference ΔV and a Q_ℓ larger than the minimum liquid flow rate attainable $Q_{\ell min}$, the liquid cone remains stable and a jet emerges from its apex. Some decades later, Cloupeau and Prunet-Foch (1994) qualitatively described the existing regimes of operation as a function of the different combinations of electrical and mechanical properties of the liquid involved (e.g. electric conductivity K, surface tension σ, density ρ_ℓ, viscosity μ_ℓ, outer and inner electrical permittivity ε_o, ε_i) so as the governing dynamical inputs (e.g. liquid flow rate Q_ℓ and voltage difference ΔV). Particularly, the cone-jet mode has been and remains the main regime used due to its inherent steadiness, robustness and its relatively high monodispersity ratio. Note that steadiness is not only a characteristic of the hydrodynamic field, but also in terms of the spatial distribution of the electrical charge.

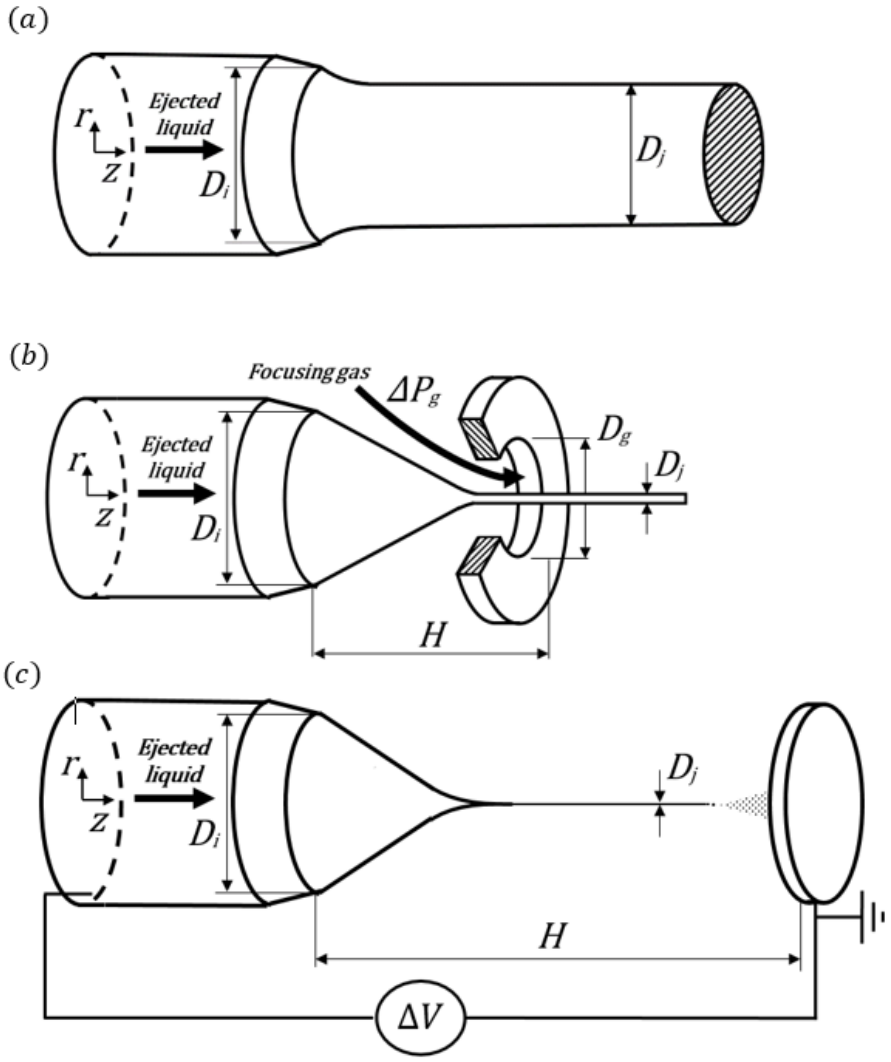

Figure 1.3: Sketches of liquid jets produced by (a) inertial ejection without any pulling assistance; (b) a flow focusing nozzle, where the liquid ejection is assisted by a gas pressure ΔP_g through a little hole downstream; and (c) electrospray, where the driver comes from highly intense electric fields produced by a voltage difference ΔV.

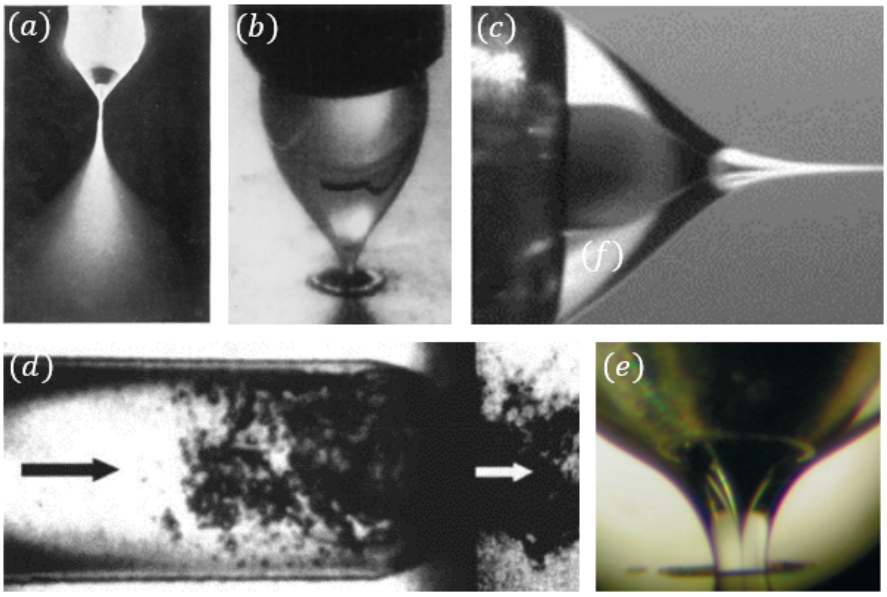

Figure 1.4: Production of liquid jets and drops ir air or vacuum ambient: (a) One of the first photographs of Electrospray, where cone, jet and the droplet plume are shown. (b) One of the first photographs of flow focusing where a stretched meniscus is shown (c) Coaxial electrosprayed liquid jets for micro-encapsulation . (d) Flow focusing diverging to Flow Blurring, where stable menisci are prevented to be by the formation of an unstable turbulent air-liquid mixture that forms an fine spray ejected downstream. (e) Double gas-liquid flow focusing. (a) Reprinted with permission from (Zeleny, 1917). Copyright (1917) by the American Physical Society. (b) Reprinted with permission from (Gañán-Calvo, 1998). Copyright (1998) by the American Physical Society. (c) From (Loscertales *et al.*, 2002). Reprinted with permission from AAAS ©2002. (d) Reprinted from (Gañán-Calvo, 2005), with the permission of AIP Publishing (e) Reprinted by permission from Springer Nature: Springer. Nature Physics (Gañán-Calvo *et al.*, 2007) ©2007.

Now, we bring up the classical Nernst-Planck differential equation for the concentration of a certain ionic species n_k and its evolution as a function of an applied electric field E, thermal diffusivity D_k and the rate of

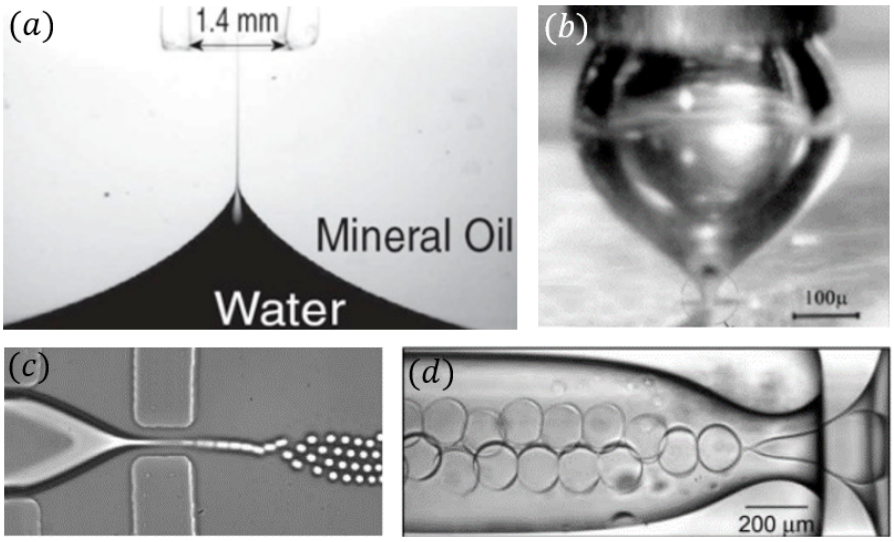

Figure 1.5: Emulsions and bubbles generated by flow focusing configurations: (a) Selective withdrawal for water-oil encapsulation (b) Microbubbling production from an liquid-focused gas meniscus (c) Liquid-liquid streams for making emulsions (d) Micro-encapsulation by a double liquid-liquid nozzle. (a) From (Cohen *et al.*, 2001). Reprinted figure with permission from AAAS ©2001. (b) Reprinted with permission from (Gañán-Calvo & Gordillo, 2001). Copyright (2001) by the American Physical Society. (c) Reprinted figure from (Anna, Bentoux & Stone, 2003), with the permission of AIP Publishing. (d) From (Utada *et al.*, 2005). Reprinted figure with permission from AAAS ©2005.

production r_k by reaction r_k,

$$\frac{dn_k}{dt} = -\nabla \cdot [(w_k e z_k n_k \mathbf{E}) + D_k \nabla n_k] + r_k \tag{1.4}$$

where e is the elementary charge and w_k, z_k are the mobility and the valence of the specie k, respectively. From a macroscopic point of view and taking the global density $\rho_e = \sum_k \rho_{e,k} = \sum_k F z_k n_k$ and the sum of charge production rates of the k-species $\xi = \sum_k F z_k r_k$ (i.e. F is the Faraday constant), we can obtain the following expression,

$$\frac{d\rho_e}{dt} = -\nabla \cdot (K\mathbf{E}) + \sum_k D_k \nabla^2 \rho_{e,k} + \xi \tag{1.5}$$

whose terms are generally of the same order of magnitude.

On the one hand, the balance between the electric drift and the thermal diffusion $K\rho_e/\varepsilon \sim \nabla\cdot(k\mathbf{E}) \sim \sum_k D_k\nabla^2\rho_{e,k} \sim D_d\Delta\rho_e/\lambda_D^2$ (i.e. assuming a characteristic variation of charges $\Delta\rho_e$ along the Debye length λ_D), leads to a scale for the Debye length as $\lambda_D = (\varepsilon D_d/K)$. On the other hand, the temporal variation and the electric lift term are balanced, whose scales provides an estimates for the electrical relaxation time $t_e = \varepsilon/K$. Fortunately, there exist conditions for jumping from an electrokinetic description to a more simplified modeling, the Taylor-Melcher model or the leaky dielectric model Saville (1997). The latter model assumes that the diffusion current is significantly smaller than the conduction one. This allows us to consider a constant conductivity K in bulk. To apply this condition, the imposed electrical field must be constrained by the thermal voltage V_T through the Debye layer and the fluid length scale as the upper and lower limit, respectively. This entails

$$\frac{\varepsilon D_d}{K} = \lambda_D \ll \frac{V_T}{E} = \frac{k_B T}{eE} \ll a \tag{1.6}$$

and logically leads to a Debye length λ_D much smaller than the characteristic fluid length scale a. Note that k_B, T and e are the Boltzman constant, the temperature and the elementary charge. Previous conditions together with the temporal constraint given by $t_e/t_h \ll 1$, enables as to consider a quasi-instantaneous allocation of charges from the bulk to the surface (i.e., the hydrodynamic residence time $t_h = a/v_f$ is much larger than t_e). So, the Taylor-Melcher approach (Saville, 1997) can be adopted and an electrical balance can be rigorously derived in terms of a surface charge density ρ_{es} as

$$\frac{d\rho_{es}}{dt} = -\left\| K\mathbf{E} + \sum_k D_k\nabla\rho_{e,k} \right\| \cdot \mathbf{n} + \rho_{es}\mathbf{n}\cdot(\mathbf{n}\cdot\nabla)\,\mathbf{v_f} \tag{1.7}$$

where $\mathbf{n}$ is the normal vector to the surface and, all the variables are evaluated at the own surface and $\|\|$ denotes the normal variation of the terms inside it through the surface.

Interestingly, steady electrospray is found to be under previous relaxed constraints of the leaky dielectric model. Several groups have intensively studied the governing laws of electrospray for the last three decades with a great controversy in the field. Recently, Gañán-Calvo's school of thought

demonstrated with energetic arguments that their theory is better physically founded than others (Gañán-Calvo & Montanero, 2009). At first order, the kinetic energy of the jet $\rho_\ell v_j^2 Q_\ell$ is balanced to the electric power released $\Delta V \cdot I$, being v_j the jet speed. We can assume that the main variations for ΔV take place along the cone-jet transition region of length L (i.e. distance from the apex to the region where the jet diameter remains approximately constant). Besides, the electric current can be estimated as $I \sim K D_j^2 E_s \sim K D_j^2 \left(\sigma/\varepsilon_o L\right)^{1/2}$. Note that E_s is the tangential electric field on the jet surface, which commensurate to the normal component $E_{n,cone}$ at the cone surface. Consequently, the previous balance provides a scaling law for the jet diameter D_j^{ES}:

$$D_j^{(ES)} \sim \left(\frac{\rho_\ell Q_\ell^3 \varepsilon_o}{\sigma K}\right)^{1/6} \tag{1.8}$$

This conclusion would be somehow anticipated by Gañán-Calvo (2004a), through the balance of dominant forces projected on a slender scheme for each parametric regime of electrospray:

$$\frac{d}{dz}\left(\frac{\sigma}{\eta}+\frac{1}{2\pi^2}\frac{\rho Q^2}{\eta^4}\right)+\frac{6\mu Q}{\pi\eta^2}\frac{d}{dz}\frac{d\eta}{\eta dz}=\frac{2\varepsilon_0 E_n E_s}{\eta}+\frac{\varepsilon_0}{2}\frac{d}{dz}\left[E_n^2+(\beta-1)E_s^2\right] \tag{1.9}$$

where we can distinguish the different forces (from left to right) surface tension, kinetic energy, viscosity sink, electrostatic and polarization forces. Following this energetic philosophy, first order scaling laws can be also derived for flow focusing, where only mechanical power sources are present. In this sense, the power from exerted by the driving pressure $\Delta P \cdot Q_\ell$ is balanced to the kinetic energy $\rho_\ell v_j^2 Q_\ell$ transported by the jet, leading to:

$$D_j^{(FF)} \sim \left(\frac{\rho_\ell Q_\ell^2}{\Delta P}\right)^{1/4} \tag{1.10}$$

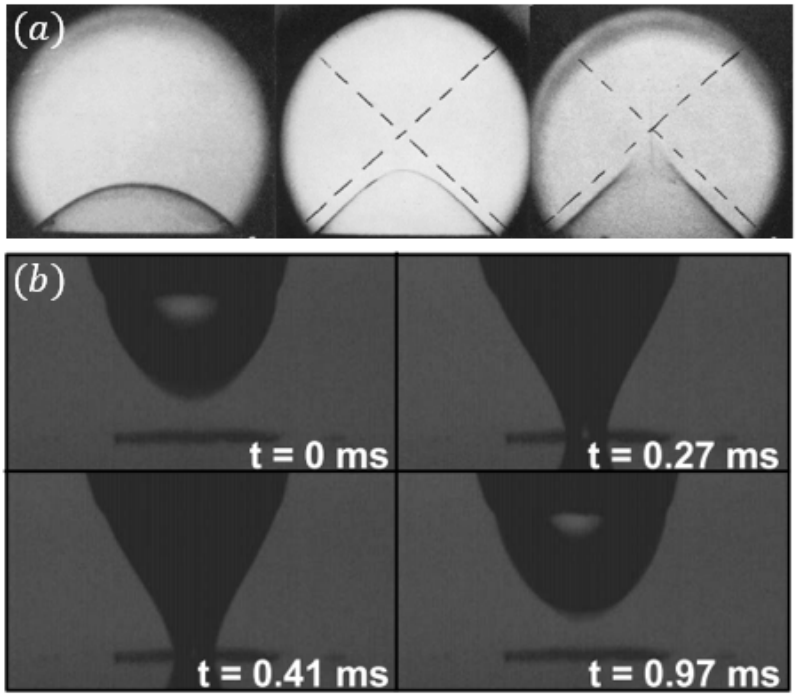

Figure 1.6: The onset of liquid conical shapes. (a) From left to right (exposure time: 1.6 ms): a how a meniscus is adopting a conical shape due to the presence of strong enough electric fields. (b) Frames of unstable dripping for a gas-focused liquid configuration. (a) Republished figure with permission of Royal Society of London, from (G. I. Taylor, 1964). Permission conveyed through Copyright Clearance Center, Inc. (b) Reprinted figure with permission from (Montanero, 2011) Copyright (2011) by the American Physical Society.

Since those previous scaling laws are valid for the steady jetting mode in both configurations, one could wonder what are the threshold values for the transition between dripping and jetting modes (see Fig. 1.6). This is interesting itself, because it is intimately linked to the minimum liquid flow rate attainable $Q_{\ell min}$ that leads the smallest droplet diameter reachable for a set of governing and parametric conditions. In the Chapters 3 and 4, we will come back to this problem for providing the relation between diameter and velocity of the jet at the dripping-jetting instability.

For the interested reader, note that an electrokinetic modeling turns

out essential for the description of transient cone-jet formation because of $t_e \sim t_h$. L. Rayleigh (1882) introduced the process and obtained a threshold for the electrical charge that a drop with a diameter D_d can transport without any fission, $q_R = \left(\varepsilon_o \sigma D_d^3\right)^{1/2}$. Essentially, he balanced the surface tension and the electrical repulsion forces at the surface of a perfect conductor drop. But, what occurs if the drop is not a perfect conductor? In this case, the migration of charges from the bulk to the surface would not be instantaneous and may plays some role in the process. For giving answer to the previous question, Collins, Sambath, Harris, and Basaran (2013) performed numerical simulations according to the Taylor-Melcher scheme (Saville, 1997). They studied how an isolated drop is deformed by the presence of a electrical field until its fission. Interestingly, they found out that the maximum charge in a drop without any fission is strongly related to the classical limit proposed by Rayleigh. Indeed, the rate would be universal and its value is 0.44. However, two parallel and independent works realized by Gañán-Calvo, López-Herrera, noz, and Montanero (2016) and Pillai, Berry, Harvie, and Davidson (2016) demonstrated that the previously derived universal value is not congruent with a more detailed numerical simulations where electrokinetic effects are included by an averaged-electrical-conductivity electrokinetical model (López-Herrera et al., 2011), (López-Herrera et al., 2015) and a pure electrokinetical model (Berry et al., 2013), respectively. Indeed, Gañán-Calvo et al. (2016) found the fitting that would confirm their asseverations:

$$\frac{q}{q_R} = 0.5 \left(\frac{\mu_\ell^{12}}{\rho_\ell^{10} \sigma^{10} K^4 \varepsilon_o^5 \varepsilon_i^3} \right)^{1/72} \neq 0.44 \tag{1.11}$$

1.3 The delivery of biomolecules at XFELs

Elemental bricks of the life are mainly formed by macromolecules as proteins, lipids or nucleic acids and their essential functionality in living cells. The ample variety of molecular structures makes possible a differentiation of the roles involved in physiological mechanisms. So, knowing the architecture of molecules at a great degree of detail turns out essential for opening new avenues in biology or drug design as well. In this section, we will illustrate how X-ray Free-Electron Lasers enables molecule structure determination with atomic resolution. These possibilities were suggested

by Neutze, Wouts, Spoel, Weckert, and Hajdu (2000) through some numerical simulations on the energetic interaction between an incident X-ray beam and a certain aggregate of molecules. Surprisingly, its structural integrity was kept during approximately the first ten femtoseconds of the energetic dose (see Fig. 1.7).

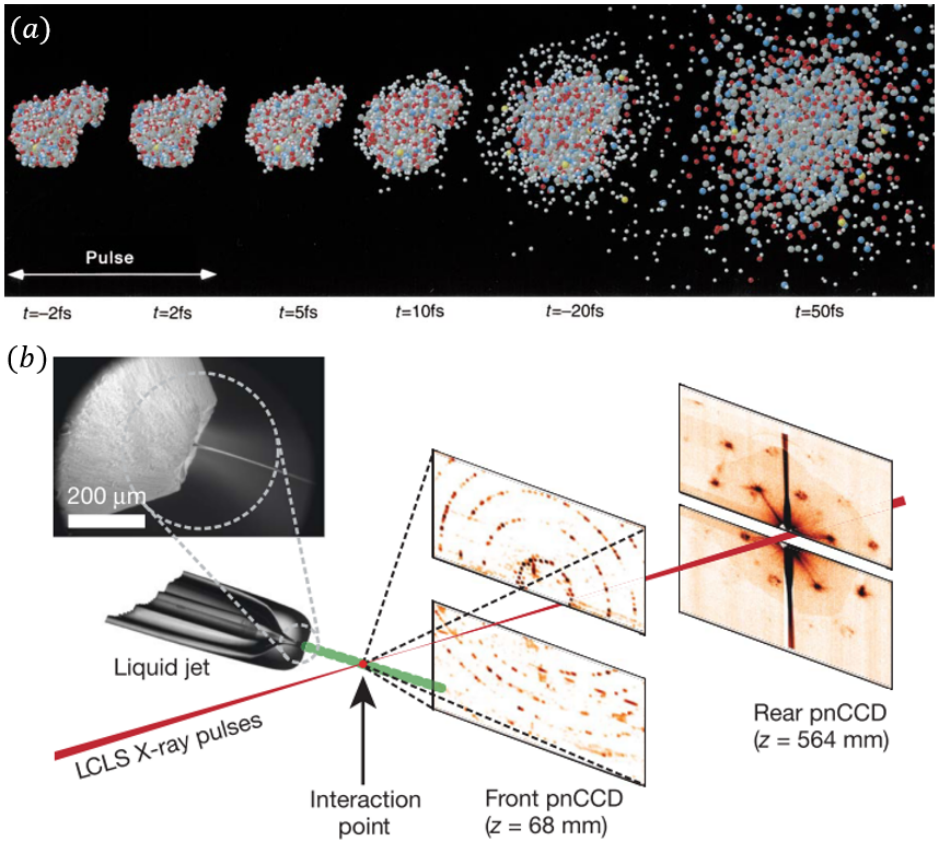

Figure 1.7: Illustrations of the diffraction before destruction concept in both (a) the seminal numerical simulation of the macromolecule structure evolution under the action of a laser pulse and (b) the seminal experimental method of Serial Femtosecond Crystallography with the use use LCLS XFEL pulses and gas-focused liquid jets for delivering micro-crystals that contain biomolecules. (a) Reprinted by permission from Springer Nature: Springer. Nature. (Neutze *et al.*, 2000) ©2000. (b) Reprinted by permission from Springer Nature: Springer. Nature. (Chapman, 2011 *et al.*) ©2011.

As the duration of XFEL pulses has that timescale, they suggested their use for collecting diffraction patterns within that temporal interval when molecules are not damaged yet.

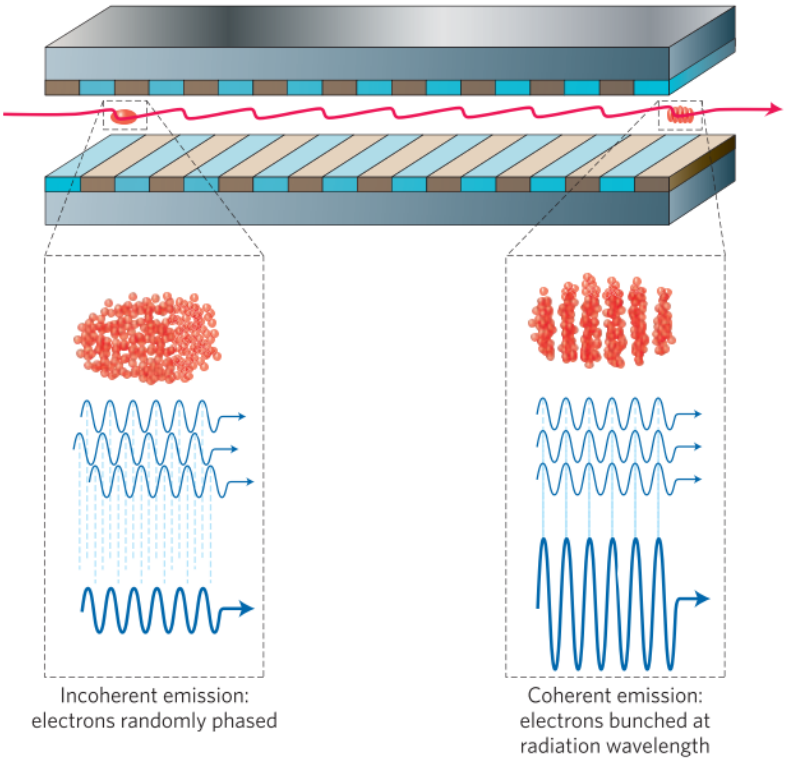

Figure 1.8: FEL operating principle. Reprinted by permission of Springer Nature: Springer. Nature Photonics. (Macneil & Thompson, 2010).

For the interested reader, we include a brief explanation about the physical principle of free-electron lasers (Pellegrini *et al.*, 2016). Essentially, we need an accelerated beam of electrons that reaches approximately the speed of light. At those conditions, we force that the beam of electrons to enter an undulator with random phases (see Fig. 1.8). Then they interact in a collective way with their own radiation, which makes the small coherent fluctuations in the radiation field grow and simultaneously begin to bunch the electrons at the resonant wavelength. This global process keep going until the bunch is very strong and the process satu-

rates with a power several orders of magnitude larger than the undulator radiation (Mcneil & Thompson, 2010).

Serial Femtosecond Crystallography - Almost a decade later, (Chapman *et al.*, 2011) demonstrated experimentally the diffraction-before-diffraction concept, where the high brilliance of XFEL pulses enables the diffraction from micro-crystals and patterns can collected before their damage. This was early corroborated by additional works in that first stage of the technology (Boutet et al., 2012; Seibert *et al.*, 2011). Those Bragg peak intensities can be analyzed through the convergence of computational algorithms for ensuring a high accuracy of the three dimensional molecular model obtained (White *et al.*, 2012, 2016). A proper mapping of the molecule structure orientation demands typically the record of some thousands of diffraction patterns to ultimately resolve it. Thus, a serial delivery of biomolecules was the strategy followed in that seminal article. Specifically, a customization of the original flow focusing nozzle (Gañán-Calvo, 1998) was realized by DePonte et al. (2008) (also called as GDVN). Due to its great robustness and friendly command, flow focusing has been extensively used as the standard vehicle for transport of micro-crystals in SFX experiments. However, each study has its own specifications and requirements which demand particular features to the liquid delivery. Thus, SFX community has invested many efforts for further developments in liquid injection. For instance, Sierra *et al.* (2012, 2015) proposed the use of electrospinning for SFX (called MESH in the field) in order to reduce the sample consumption, a shared goal for double flow focusing (Oberthür *et al.*, 2017) or acoustic droplet ejection as well (Roessler *et al.*, 2016). Note that the latter method would demand the frequency of both XFEL pulses and droplet trains. In the Chapter 2, we will analyze how flow focusing can cover the features of the latter method without any external excitation. On the other hand, Weierstall *et al.* (2014) introduced their LCP extrusion injector for analyzing membrane proteins such as microbial rhodopsins (Pebay-Peyroula, 1997) and G protein-coupled receptors (Cherezov *et al.*, 2007) among others. Since previous methods landed at SFX experiments, some improvements have been proposed so far. In terms of manufacturing, we can find several techniques: soft-lithography (Trebbin et al., 2014), ceramic injection (Beyerlein *et al.*, 2015), highly-reproducible nano 3D printing (Nelson *et al.*, 2016a) and combinations with lab on a chip solutions (Bohne *et al.*, 2019) among others.

Nowadays, more challenges are arising for the sample delivery. They were recently addressed by Stan *et al.* (2016), showing experimentally how liquid jets and drops interacts with XFEL pulses. Essentially, they explored the gap dynamics of the liquid $2X(t)$ that occurs after a XFEL pulse vaporizes the neighbor of the interaction point (see Fig. 1.9). Basically, they distinguish among three stages as follows: (I) generation of water films from the vaporization process at velocities v_{gas}, where the half gap growth X_I has this temporal dependence

$$X_I = \frac{D_j}{2} + C\frac{D_j}{2}\log(1+\frac{t}{t_I}) \tag{1.12}$$

and D_j, C and $\tau = D_j/2v_{gas}$ are the jet diameter, a dimensionless constant around unity and a characteristic time, respectively. They also goes in depth, distinguishing between a low l and high h pressure regimes in terms of the empirical relation for the characteristic pressure $P_{Sr} = \rho_\ell(c_o + 2u_P)u_P$, where ρ_ℓ is the liquid density, c_o the speed of sound in water and u_P as the particle velocity, with $P_{Sr} \propto u_P$ and $P_{Sr} \propto \sqrt{u_P}$ for $P_{Sr} < 10GPa$ and $P_{Sr} > 1GPa$, respectively. So, for both regimes, C and τ are:

$$C_l = \sqrt{\frac{\rho_L c_o^2}{\delta_L}}\frac{\sqrt{K_{E,l}}}{K_{v,l}}, \quad t_{I,l} = \frac{2}{3}\frac{D_j^3}{8K_{v,l}}\frac{\pi\rho_L c_o}{E_{Xray}\alpha_{Xray}\Gamma} \tag{1.13}$$

$$C_h = \frac{\sqrt{K_{E,h}}}{\sqrt{2}K_{v,h}}, \quad t_{I,h} = \frac{D_j^2}{4K_{v,h}}\sqrt{\frac{\pi\rho_\ell}{3E_{Xray}\alpha_{Xray}\Gamma}} \tag{1.14}$$

where E_{Xray}, α_{Xray}, δ_L are the pulse energy, the X-ray absorption coefficient and the cohesive energy density of water, respectively, so as Γ is the Gruneisen coefficient (e.g., 0.5 for liquid water at densities around 1 kg/m^3) and the fitting coefficients with values $K_{E,l} = 0.08$, $K_{v,l} = 0.21$, $K_{E,h} = 0.06$, and $K_{v,h} = 0.12$ for flow focused water jets. (II) An intermediate case that occurs between the vaporization finishes and the liquid film coalesces with the jet. (III) When the debris has already disappeared. For the stages (II) and (III), the retraction velocity of the jet is $v_r = (8\sigma/\rho_\ell D_j)^{1/2}$ at first order and according with experimental measurements. This is congruent with the resulting capilar velocity from the

balance between the kinetic energy convected by the jet and the surface tension force contribution $1/2\rho_\ell v_c^2 = 2\sigma/D_j$.

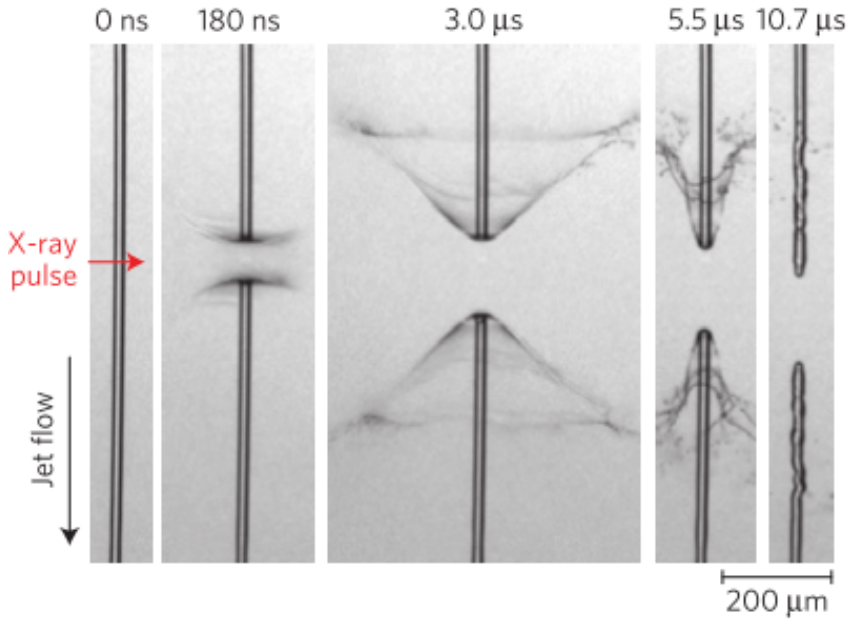

Figure 1.9: Snapshots of the energetic interaction between a X-ray FEL pulse with a liquid jet. Reprinted by permission of Springer Nature: Springer. Nature Physics. (Stan *et al.*, 2016).©2016.

Likewise, the maximum half gap sizes at the end of the stage I comes from the balance between the capillary wave and the retraction velocity, which leads to

$$X_{I,l}(t_I^{end}) = \frac{D_j}{2} + \frac{D_j}{2}\sqrt{\frac{\rho_\ell c_o^2 K_{E,l}}{\delta_L K_{v,l}^2}}\log\left(\sqrt{\frac{2K_{E,l}}{\sigma\delta_L}}\frac{E_{Xray}\alpha_{Xray}\Gamma}{\pi D_j^{3/2}}\right) \quad (1.15)$$

$$X_{I,h}(t_I^{end}) = \frac{D_j}{2} + \frac{D_j}{2\sqrt{2}}\frac{\sqrt{K_{E,h}}}{K_{v,h}}\log\left(\sqrt{\frac{K_{E,h}}{8\pi}\frac{6E_{Xray}\alpha Xray\Gamma}{\sigma D_j}}\right) \quad (1.16)$$

A simple criterion for choosing either low ($P_{Sr} < \delta_L$) or high $P_{Sr} > \delta_L$ pressure approaches is given by the experimental collapse of data for different

parametric conditions. Now, we are ready to extract conclusions from the previous equations concerning to the work of Stan *et al.* (2016). Given a fixed frequency between pulses f_{XFEL}, we intend to provide some criteria for ensuring an interaction between the laser beam and the liquid jet for each XFEL pulse delivered. This imposes a jet velocity of design v_j^{req}. Firstly, we need to know the duration of the stage I ($t_{I,end}$) for both asymptotic models in gas pressure. Some algebraic manipulations in equations lead to

$$v_j^{design} = \frac{D_j}{2} f_{XFEL} \left[1 + C \log \left(1 + \frac{1}{f_{XFEL} \tau(D_j)} \right) \right], \quad if \quad f_{XFEL} \gtrsim \frac{1}{t_I^{end}} \tag{1.17}$$

where the end time for the stage I has the following expression:

$$\frac{t_I^{end}}{t_I} = \exp \left[\frac{2X_I(t_{I,end})}{CD_j} \right] - 1 \tag{1.18}$$

Substituting the different expressions into the equation for v_j^{design}, we can observe a quasi-linear dependence $v_j^{design} \propto D_j$ if it is assumed that logarithmic term is of the order of unity. Since the generation of high speed jets is a challenge, then it would be convenient to minimize v_j^{design} and consequently, to decrease D_j as much as possible. So, the jet speed required would turn out smaller for getting a full replenish of hte gap before the next XFEL arrives. This is why the larger f_{XFEL} is, the larger is v_j^{design}. In any case, besides the optimization of the jet speed for SFX experiments, jet diameter should be compatible with the size of the crystal to be smoothly transported.

Another function to be maximized is the crystal hit rate h_r. For a certain beam pulse diameter D_{BP}, we have to evaluate the interaction region between the XFEL pulse (B) and the liquid jet (J). The intersected volume has a typical crossed section S_{int} and a diameter D_{int}. Given a certain dilution of crystals dil_c in the liquid and assuming a homogeneous crystal distribution, the percent of hit rate would turn out approximately $h(\%) \sim 100 \cdot D_{int} S_{int} / dil_c \%$. So, the dimensional hit rate has this expression $h_r = h(\%) \cdot f_{XFEL} / 100$. We have two different situations for the estimation of D_{int} and S_{int}, and consequently for h_r:

- $D_j \ll D_{BP}$ (see Fig. 1.10): $D_{int} \sim D_j$ and $S_{int} \sim D_j \cdot D_{BP}$, which leads to

$$h_r^{(J \ll B)} \sim \frac{D_j^2 D_{BP}}{dil_c} f_{XFEL} \tag{1.19}$$

- $D_j \gg D_{BP}$: $D_{int} \sim D_{BP}$ and $S_{int} \sim D_j \cdot D_{BP}$, which leads to

$$h_r^{(J \ll B)} \sim \frac{D_j D_{BP}^2}{dil_c} f_{XFEL} \tag{1.20}$$

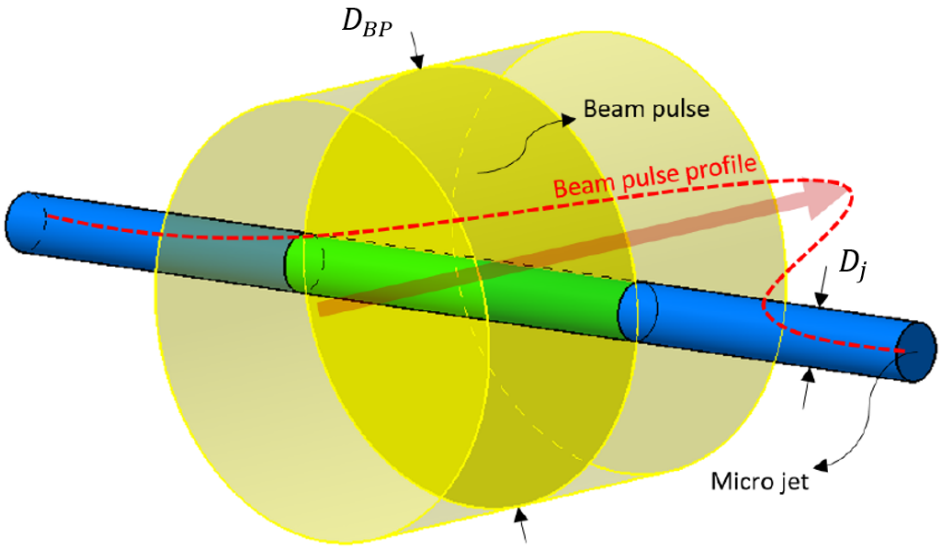

Figure 1.10: Case of a XFEL beam pulse (yellow color) of diameter D_{BP} that hits a much thinner liquid micro-jet (blue color) of diameter D_j. The interaction is depicted in green.

The advent of high-pulse rate facilities such as European XFEL (4.5 MHz-in-bunch) and LCLS II (1 MHz) makes critical the fulfillment of previous requirements for taking advantage of the full capabilities that these XFEL facilities offer. In this sense, we will explore the use of flow focusing for megahertz SFX experiments in the last section of the Chapter 3, which is fruit of an international collaboration of numerous groups according to the proposal XFEL2012 led by Prof. H. N. Chapman and Dr. A. Barty.

Single Particle Imaging - The enormous investment on the development of LCLS II and European XFEL has enabled a big increase of the energetic dose at ultra-short rates. This enhancement has allowed the scientific community to dream for taking images of weakly scattering particles without any crystallization. Under these conditions, the reduction of the background scattering from the liquid turns out even more crucial for single particle imaging (SMI) than that for typical SFX experiments. This leads to minimizing the thickness of the liquid around the sample. Regarding the injection method, most of the attempts have been performed with aerosolized liquid streams. So, the XFEL beam would be focused on the cloud of droplets ejected. Unfortunately, the hit rate obtained for both liquid and sample turns out very low if it is compared with an analogous experiment of SFX with steady liquid jets at larger scales. One could

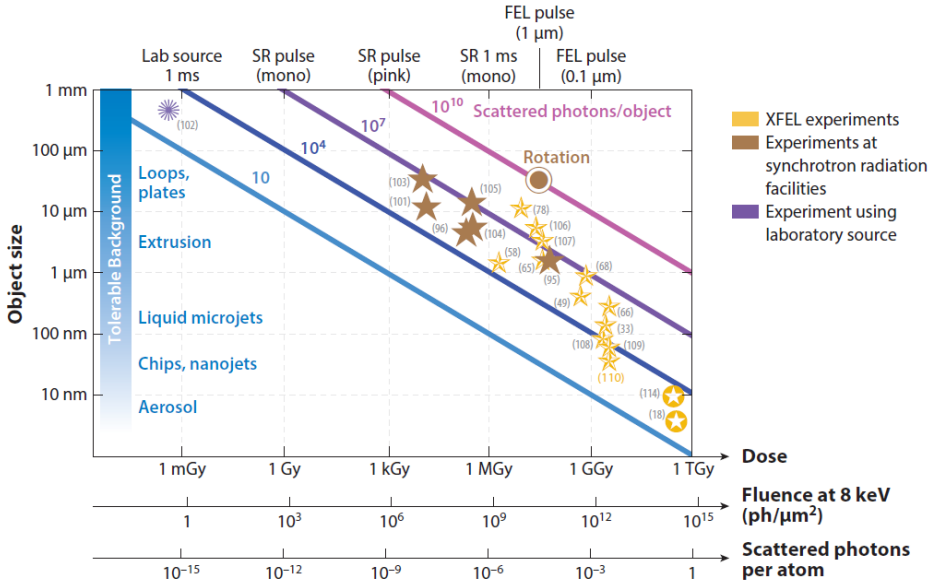

Figure 1.11: Performance of X-ray FEL sources, synchrotron facilities and laboratory-scaled experiments as a function of the object size, the dose with the corresponding fluence and scattered photons per atom. Reprinted by permission from ANNUAL REVIEWS: Annual Review of Biochemistry. (Chapman, 2019)©2019.

wonder what reasons have prevented the application of steady liquid jets at the smaller scales required. The root of the problem comes from the

appearance of instability mechanisms and loosing of robustness at those operational conditions (e.g., D_j ranging from some decades to some hundreds of nanometers) (see Fig. 1.11). This also entails a compromise between the jet features and the feasibility of the nozzle fabrication. This is a matter for the Chapter 4, where a novel way will be introduced for its potential use at SMI experiments. Interestingly, scaling laws will be also derived for this kind of extreme conditions, where the speed and diameter of the jet should be maximized and minimized, respectively.

1.4 What works compose this Ph. D. thesis?

The results and concepts that will be shown along this thesis are partially based on the following published works where the PhD candidate is main author or participated as co-author. So, the PhD candidate has a h-index=4, with 26 citations (Scopus: April, 2019). Total citations/total articles=6.5.

Research articles as main author:

- F. Cruz-Mazo, J. M. Montanero, A. M. Gañán-Calvo (2016) "Monosized dripping mode of axisymmetric flow focusing" Phys. Rev. E., with permission from American Physical Society for its partial or total reproduction in this thesis. Impact factor: 2.366 (Q1: 6 of 53 in category of Physics, Mathematical) (Source: Journal Citation Reports, 2016) Citations: 7 (Source: Scopus, April 2019)

- F. Cruz-Mazo, M. A. Herrada, A. M. Gañán-Calvo, J. M. Montanero (2017) "Global stability of axisymmetric flow focusing" J. Fluid Mech. with permission from Cambridge University Press for its partial or total reproduction in this thesis. Impact factor: 2.893 (Q1: 16 of 134 in category of Mechanics) (Source: Journal Citation Reports, 2017)

- F. Cruz-Mazo, M. O. Wiedorn, M. A. Herrada, S. Bajt, H. N. Chapman, A. M. Gañán-Calvo (2019) "Aerodynamically-assisted electrified microscopic jets" in preparation for resubmission.

Research articles as co-author:

- M. O. Wiedorn *et al.* (2018) "Rapid sample delivery method for megahertz serial crystallography at XFELs" IUCRJ with permission from IUCRJ for its partial reproduction in this thesis. Contribution of the Ph. D. candidate: experimental work and theoretical discussions. Impact factor: 6.544 (Q1: 3 of 26 in category of Crystallography) (Source: Journal Citation Reports, 2017) Citations: 5 (Scopus: April, 2019)

- M. O. Wiedorn *et al.* (2018) "Megahertz serial crystallography" Nat. Commun. with permission from Springer Nature for its partial reproduction in this thesis. Contribution of the Ph. D. candidate: experimental work as member of the injection team led by Dr. M. O. Wiedorn and Dr. S. Bajt. The proposal (XFEL2012) was globally led by Prof. H. N. Chapman and Dr. A. Barty. Impact factor: 12.353 (D1: 3 of 64 in category of Multidisciplinary) (Source: Journal Citation Reports, 2017) Citations: 9 (Scopus: April, 2019)

- A. M. Gañán-Calvo, H. N. Chapman, M. Heymann, M. O. Wiedorn, J. Knoska, Y. Du, B. Ganan-Riesco, M. A. Herrada, J. M. López-Herrera, F. Cruz-Mazo, and S. Bajt "Steady capillary jet length" in preparation for submission. Contribution: experimental work and theoretical discussions.

Invention patent as co-inventor:

- A. M. Gañán-Calvo, F. Cruz-Mazo, A. J. Díaz-Quintana, I. Díaz-Moreno, B. Ganan-Riesco, M. O. Wiedorn, H. N. Chapman, S. Bajt

(2018) ”Aerodynamically-stabilized electrified microscopic liquid jets for the transport of samples” Pub. No. US 2018 / 0348091 A1. Filed: Jun. 1. 2018. Published: Dec. 6. 2018.

Chapter 2

Droplets periodically delivered by gas-focused liquid menisci

> Each piece, or part, of the whole of nature is always merely an approximation to the complete truth, or the complete truth so far as we know it. In fact, everything we know is only some kind of approximation because we know that we do not know all the laws as yet.
>
> Richard P. Feynman

Since the foundational paper of Gañán-Calvo (1998), *flow focusing* has attracted the scientific community for its robustness and easy command in the production of jets and droplets at the microscale. Specifically, the majority of attention has been paid regarding how this configuration allow generate droplets small enough with a compatible frequency of generation as large as possible, keys for processes within industry such as microencapsulation, water-oil emulsions, 3D-printing among others. However, the non-linearity character of the jet breakup makes essential the appearance of satellite droplets that prevent a perfect monodisperse droplet production. In this Chapter, we will address that limitation

by the introduction of the *monosized dripping* mode of flow focusing. So, we are able to generate droplet trains with diameters significantly smaller than those produced by a typical dripping faucet (Fig. 2.1).

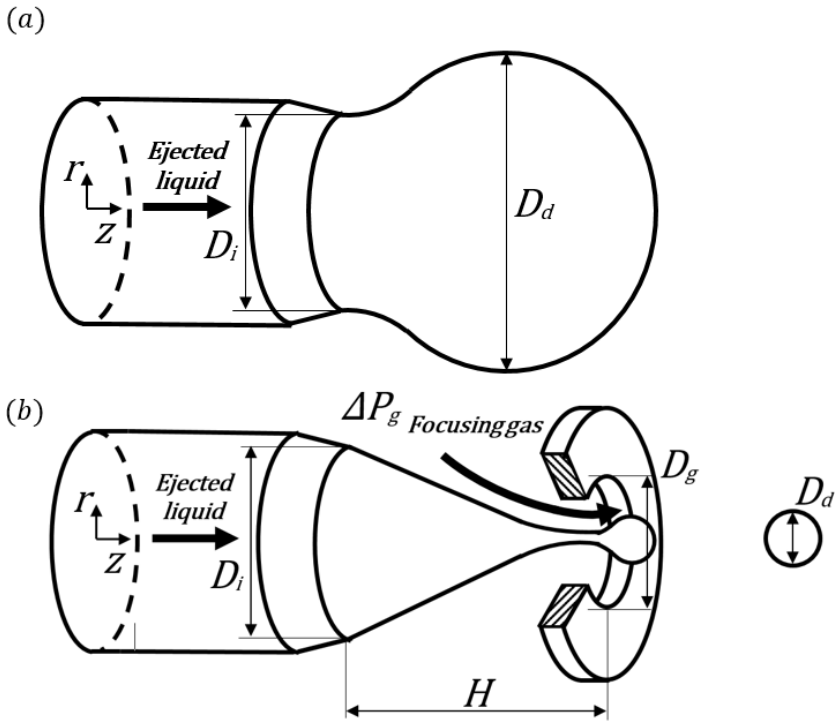

Figure 2.1: Comparison of (a) dripping faucet against (b) the *monosized dripping* mode of flow focusing.

2.1 Concept and scaling analysis

From a feeding capillary tube of diameter D_i, we inject a flow rate Q_ℓ of a liquid with a density ρ_ℓ, viscosity μ_ℓ and a surface tension σ against a wrapping gas stream of density ρ_g, viscosity μ_g that flows with a pressure gradient ΔP_g through a discharge round aperture of diameter D_g. So, these gas-liquid flows enable the ejection of droplets with diameter D_d. Let us to consider the projection of the momemtum equation over the symmetric

axis, where its evaluation reads as

$$\frac{\partial u}{\partial t}+u\frac{\partial u}{\partial z}=-\frac{1}{\rho_\ell}\frac{\partial p}{\partial z}+\frac{\mu_\ell}{\rho_\ell}\frac{\partial^2 u}{\partial z^2} \tag{2.1}$$

where u and p are the z components of the velocity and pressure in the liquid domain, respectively. Only the dominant contribution of the viscosity term has been retained, while forces with gravitational origin are neglected (i.e. $Fr \gg 1$ and $Bo \gg 1$). Taking D_i as a reference length z, a characteristic velocity $u \sim Q_\ell/D_d^2$, and a pressure gradient as $\partial p/\partial z \sim \Delta P/D_i$, we can distinguish between the firs-order scaling law that governs the droplet diameter for the steady jetting and the monosized dripping modes. For liquid flows with $We_\ell \gg 1$ and $We_\ell \lesssim 20$, steady jetting is found. Under these conditions, the jet diameter commensurates to the main drop size ejected $D_j \sim D_d$, the convective acceleration $Q_\ell^2/D_d^4 D_i$ turns out dominant over the local acceleration Q_ℓ^2/D_d^5, that will be valid as long as $D_j \ll D_i$. Consequently, neglecting the viscosity sinks given the large enough liquid Reynolds numbers $Re_\ell = \rho_\ell Q_\ell D_i/\mu_\ell D_j^3$, we can balance the pressure term to the convective acceleration and then obtaining an expression equivalent to the well-known scaling law for steady jetting of flow focusing

$$D_j^{FF} \sim \left(\frac{\rho_\ell Q_\ell^2}{\Delta P_g}\right)^{1/4} \tag{2.2}$$

where the pressure gradient can be considered sufficiently larger than surface tension forces, which entails $\Delta P \sim \Delta P_g$. In the monosized dripping mode, $D_d \preccurlyeq D_i$, which entails a sub-dominance of the convective term over the local acceleration, by the way the pulsatile feature of the flow. Neglecting the role of the energetic sinks from viscous origins (i.e. under large enough Womersley numbers $\alpha = Q_\ell D_i^2 \rho_\ell/\mu_\ell D_d^3 \gg 1$), we can balance the local acceleration to the pressure gradient terms as follows:

$$\frac{Q_\ell^2}{D_d^5} \sim \frac{\Delta P_g}{\rho_\ell D_i} \tag{2.3}$$

Besides, dimensional analysis provides an estimation for the free-surface breakup time $t_b \sim D_d^3/Q_\ell$ as the capillary time $t_b \sim t_c = \left(\rho_\ell D_d^3/\sigma\right)^{1/2}$ if it is assumed at first-order unaffected by external parameters as D_i, Q_ℓ,

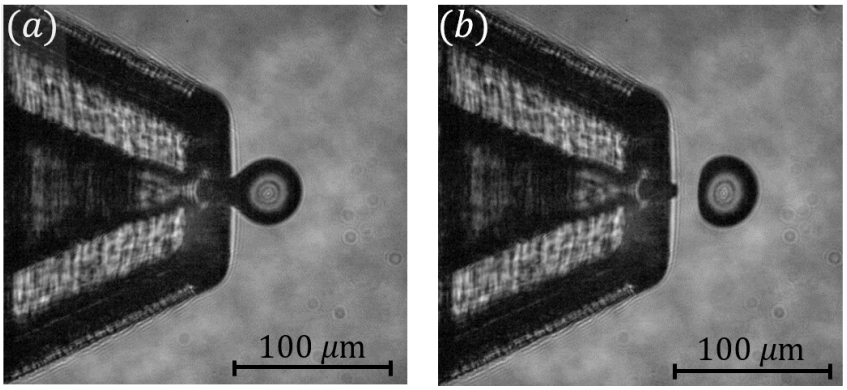

Figure 2.2: Snapshots of the *monosized dripping* and its free-satellite droplet stream liquid breakup (a) during drop inflation and (b) after drop ejection, with a diameter $D_d \sim 35$ μm for this experimental realization.

ΔP. This additional condition reduces $Q_\ell \sim \sigma^{1/2}\rho_\ell^{-1/2}D_d^{3/2}$. The latter consideration together with Eq. 2.3 allow us to derive the scaling law for the drop diameter in this mode $D_d \sim (D_i\sigma/\Delta P)^{1/2}$ and making the latter dimensionless with the length scale D_i:

$$\frac{D_d}{D_i} \sim \left(\frac{\sigma}{D_i \Delta P_g}\right)^{1/2} \tag{2.4}$$

As can be noted from Eq. 2.4, the flow rate plays a secondary role. This first-order independence assigns to Q_ℓ the role of setting a certain frequency of droplet generation and keeping the same size.

2.2 Experimental validation

We conducted experiments to validate the previously derived scaling law. We made use of two flow focusing devices with $D = 100$ μm and $H = 200$ μm and with $D = 200$ μm and $H = 100$ μm, respectively. The feeding capillary inner diameter was $D_i = 150$ μm in both cases. The liquid was injected with a syringe pump (Harvard Apparatus PHD 4400), while the air stream was supplied by a pneumatic circuit connected to a pressure regulator and a manometer. Both the air stream and the liquid droplets

are discharged to the atmosphere. The images were acquired with a high-speed camera (Hyper Vision HPV-2 Shimadzu) and processed with the open software IMAGEJ to measure the droplet diameter. We collected more than 200 experimental data using the liquids indicated in the following table.

Liquid	ρ (kg/m^3)	μ (mPa·s)	σ (mN/m)	Symbols
water	997	1	72	⬡/★
water + glycerol 50/50 vol %	1030	6.2	66	◀/▶
water + glycerol 40/60 vol %	1156	12.3	65	▼/◆
water + glycerol 30/70 vol %	1182	24.3	64	●/▲
ethanol	790	1.2	23	/■

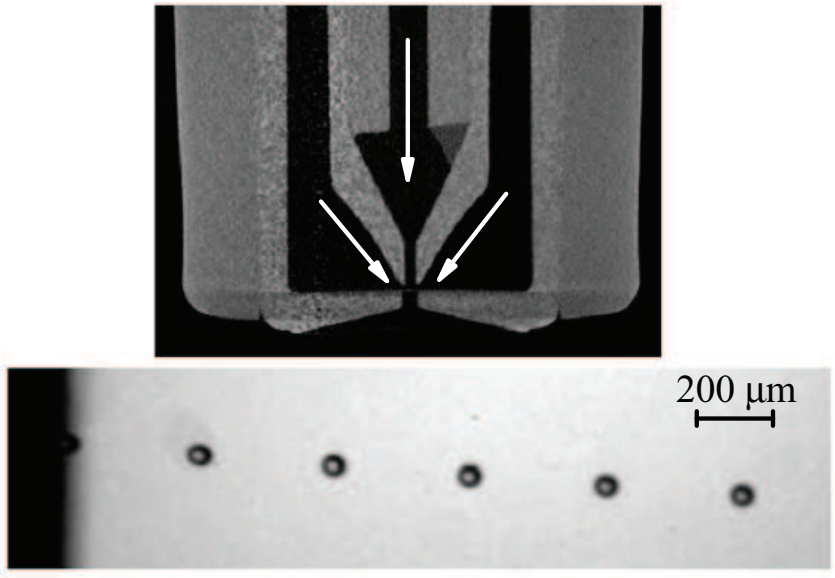

Figure 2.3: The top image is a rendering of an x-ray microtomogram of the flow focusing device with $D = 200$ μm and $H = 100$ μm. The bottom image is the monosized dripping produced with water, $Q_\ell = 25$ mL/h, and $\Delta P = 41$ mbar.

As can be observed, the viscosity ranged from low to moderately high values. In the following figure we show the parameter window where

monosized dripping was found for the least and most viscous liquids.

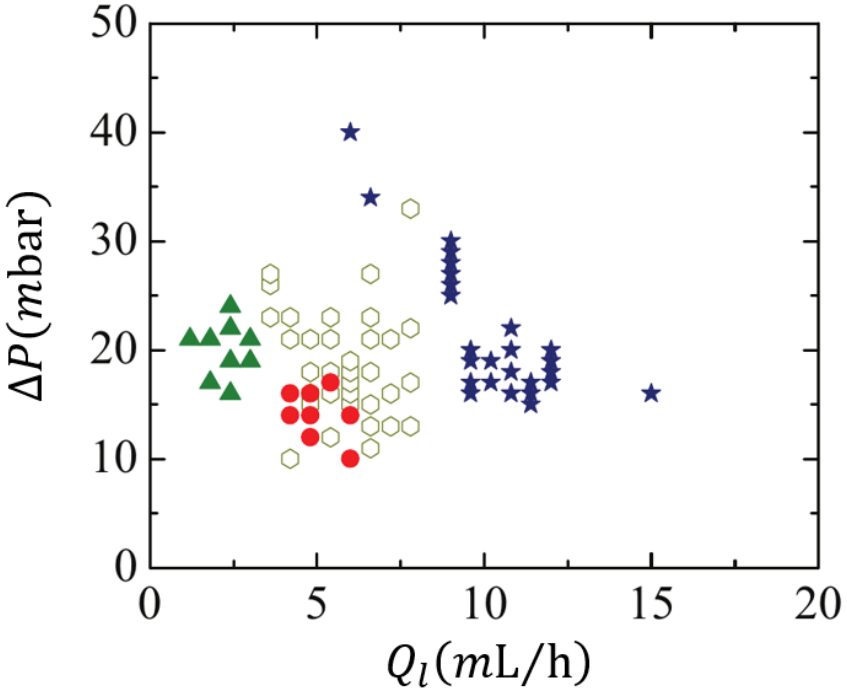

Figure 2.4: Parametrical window where monosized drippingwas found for water and water plus glycerol 30/70 vol.

The upper boundaries indicate the transition between steady jetting and monosized dripping, while the lower ones correspond to the minimum values of ΔP below which the liquid ejection interrupt. Figure shows the value of the ratio $t_c^* \sim D_d^3/Q_\ell$ and the Womersley number α in all the experimental realizations.

The approximations $t_c^* \sim D_d^3/Q_\ell$ and $\alpha \gg 1$ are consistent with most of the experimental data. It must be noted that the droplet formation starts before the free surface pinch-off begins. Therefore, the breakup time may be significantly smaller than the droplet formation time D_d^3/Q_ℓ, which explains why $t_c^* \lesssim D_d^3/Q_\ell$ (see Fig. 2.5). The diameters of the drops produced in the monosized dripping mode are shown (see Fig. 2.6). The best

fit to those diameters is the function

$$\frac{D_d}{D_i} = 1.7 \left(\frac{\sigma}{D_i \Delta P_g} \right)^{1/2} \tag{2.5}$$

with a normalized Pearson regression coefficient $R^2 = 0.913$. As anticipated from the scaling analysis, $D_d \lesssim D_i$. The scattering of the experimental data around the theoretical curve can be attributed to viscosity effects. The standard deviation of the droplet size histogram was smaller than the experimental uncertainty (around 3 %) in all the cases analyzed. We have verified that satellite droplets appear for viscosities higher than those considered in our study.

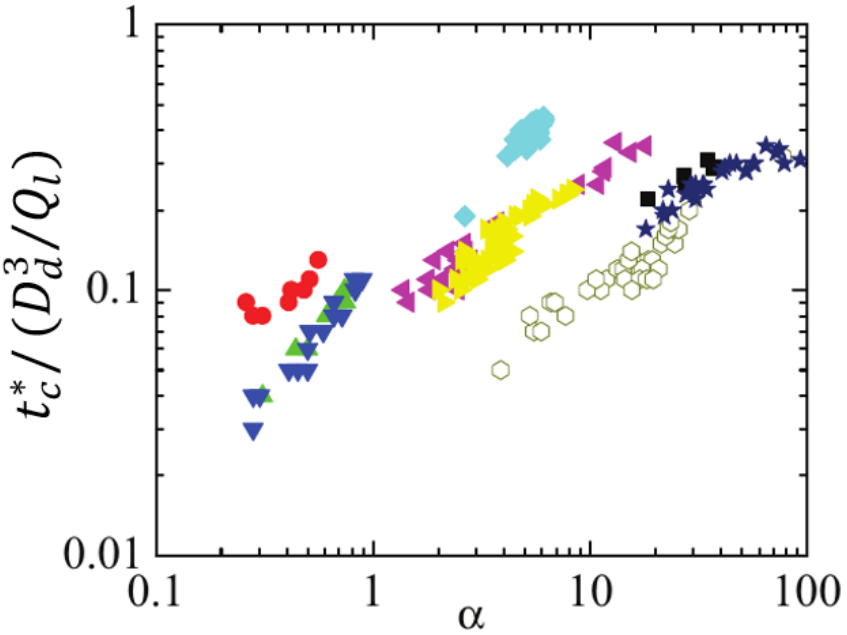

Figure 2.5: Ratio $t_c^*/(D_d/Q_\ell)$ and the Womersley number α in all the experimental realizations.

The scaling law may disguise an important aspect of the phenomenon here described: both the pressure drop ΔP and the liquid flow rate Q_ℓ are control parameters of the system.

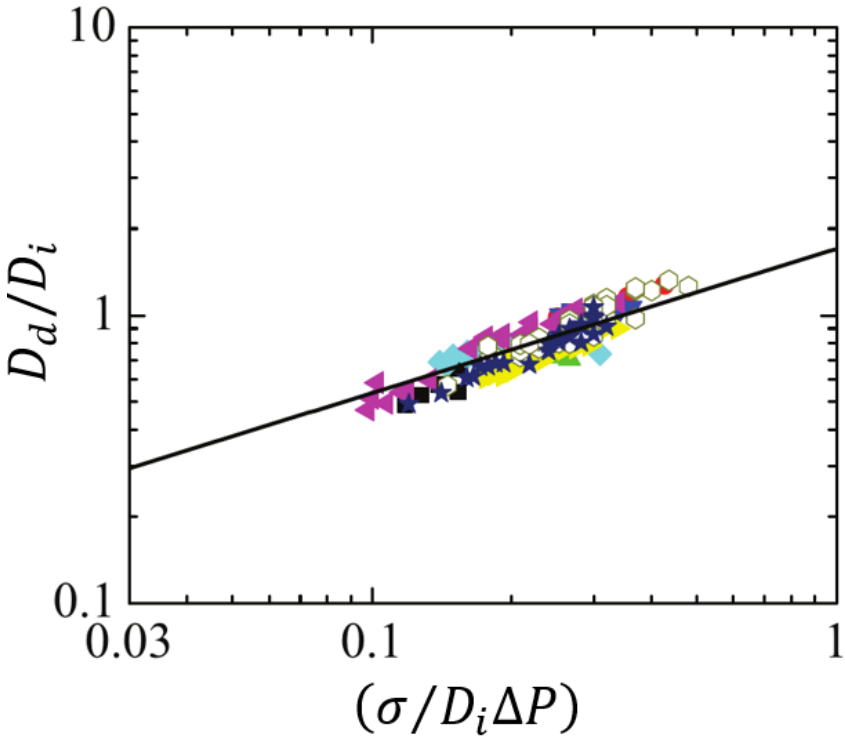

Figure 2.6: Diameters of the drops produced in the monosized dripping mode. The line is the function $D_d/D_i = 1.7(\sigma/D_i\Delta P)^{1/2}$.

Although Eq. 2.5 contains the driving pressure drop alone, the latter one and the liquid flow rate can be independently adjusted within the parameter range shown. In fact, the droplet generation frequency f can be continuously varied, without changing the droplet size, by varying the liquid flow rate while keeping the applied pressure drop constant. This implies that the droplet generation frequency does not necessarily belong to the discrete set of eigenfrequencies of the liquid meniscus. To demonstrate this, we represent in the following figure the droplet generation frequency as a function of the flow rate. The frequency was made dimensionless with the capillary time $t_c = (\rho_\ell D_i^3/\sigma)^{1/2}$ defined in terms of the feeding capillary diameter D_i, while the flow rate was expressed in terms of the characteristic quantity $Q_\sigma = (\sigma^4/\rho_\ell \Delta P^3)^{1/2}$. There is a continuous distribution of the experimental measurements along the two axes, with no trace of discontinuities associated with the discrete set of meniscus eigen-

frequencies

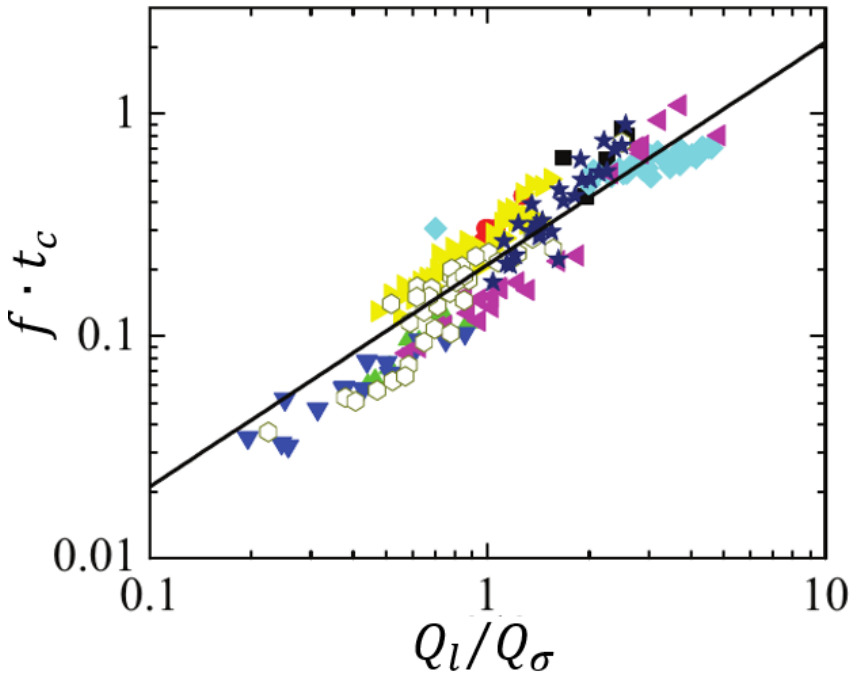

Figure 2.7: Droplet production frequency f as a function of liquid flow rate Q_ℓ. The line is the fit $f \cdot t_c = 0.21(Q_\ell/Q_\sigma)^{1.04}$ to the experimental data.

The data are fitted by a power law with exponent unity within the experimental uncertainty and therefore Eq. 2.5 is recovered.

A natural question is whether the monosized dripping mode analyzed here corresponds to the onset of the absolute instability of the flow focusing steady jetting regime and therefore the parameter conditions leading to this mode are those predicted by the spatiotemporal stability analysis of the configuration. Figure 2.8 shows all the experimental realizations projected onto the plane defined by the Reynolds and Weber numbers

$$Re_\ell = \frac{\rho_\ell v_j^{FF} D_j^{FF}}{2\mu_\ell}, \quad We_\ell = \frac{\rho_\ell (v_j^{FF})^2 D_j^{FF}}{2\sigma}, \tag{2.6}$$

where $v_j^{FF} = 4Q_\ell/\pi D_j^2$ and $D_j = (8\rho_\ell Q_\ell^2/\pi^2\Delta P)^{1/4}$ are the jet's velocity and radius calculated assuming the steady jetting regime, respectively. The figure also shows the curve corresponding to the convective-to-absolute instability transition calculated by Leib and Goldstein (1986a, 1986b). As it can be observed, monosized dripping was found for parameter conditions significantly far away from that instability transition.

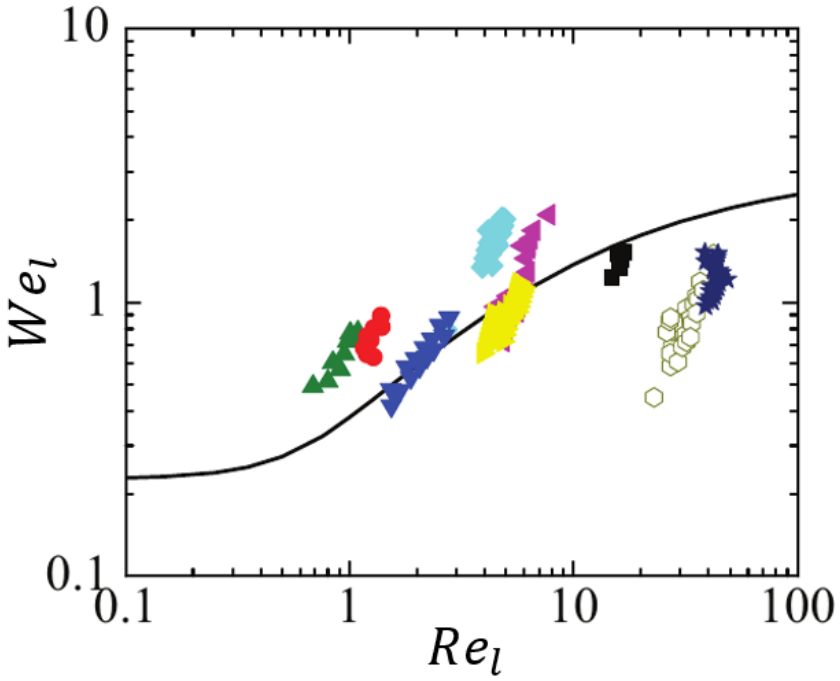

Figure 2.8: Reynolds and Weber numbers where monosized dripping was found. The curve corresponds to the convective-to-absolute instability transition described by Leib & Goldstein (1986).

In the more viscous cases, the Weber numbers were larger than those for which absolute instability arises in the jet, while the opposite occurs for the least viscous liquid. Therefore, monosized dripping is not necessarily linked to the appearance of absolute instability in the emitted jet. The fact that the monosized dripping mode is found for Weber numbers than those of the convective-to-absolute instability transition suggest that, in this case, this mode originates from an instability in the tapering meniscus (not in the emitted jet).

For the interested reader, note that the scaling law derived in this Chapter differs from that obtained for the bubbling mode of flow focusing (Gañán-Calvo & Gordillo, 2001; Gañán-Calvo, 2004b). The fact that the outer phase has a much lower density than the inner one in our system fundamentally changes the problem. In particular, while the radial pressure gradient in the outer phase can be neglected in the liquid-surrounded-by-gas system, this approximation is not valid in the opposite configuration.

Chapter 3

Gas-focused liquid jets at extreme conditions

> Divide each difficulty into as many parts as is feasible and necessary to resolve it.
>
> René Descartes

In this chapter, we analyze numerically the stability of the steady jetting regime of gaseous flow focusing. The base flows are calculated by solving the full Navier-Stokes equations and boundary conditions for a wide range of liquid viscosities and gas speeds. The axisymmetric modes characterizing the asymptotic stability of those flows are obtained from the linearized Navier-Stokes equations and boundary conditions. We determine the flow rates leading to marginally stable states, and compare them with the experimental values at the jetting-to-dripping transition. The theoretical predictions satisfactorily agree with the experimental results for large gas speeds. However, they do not capture the trend of the jetting-to-dripping transition curve for small gas velocities, and considerably underestimate the minimum flow rate in this case. To explain this discrepancy, the Navier-Stokes equations are integrated over time after introducing a small perturbation in the tapering liquid meniscus. There is a transient growth of the perturbation before the asymptotic exponential regime is reached, which leads to dripping. So, this chapter shows that flow focusing stability can be explained in terms of the combination of

asymptotic global stability and the system short-term response for large and small gas velocities, respectively.

3.1 Revision of stability and dripping-jetting

As we have introduced in the first chapter, the controlled production of liquid jets on the micrometer scale is of enormous interest in very diverse fields, such as pharmacy, biotechnology, and the food and agriculture industry. Besides the application of steady liquid jets on SFX (Chapman *et al.*, 2011), their capillary breakup is very useful for generating collimated streams of droplets, combining high production rates and good monodispersity degrees (Gañán-Calvo et al., 2013). This process requires establishing the so-called steady jetting regime, where a source of liquid steadily emits an oscillation-free filament, which eventually breaks up at distances from the source much larger than the filament diameter. If the steady jetting regime is unstable, small-amplitude perturbations grow and eventually leave the linear regime. When the nonlinear terms of the hydrodynamic equations manage to stabilize those perturbations, the instability manifests itself as self-sustained oscillations of the entire system (Sauter & Buggisch, 2005; Rubio-Rubio et al., 2013), which may give rise to non-regular emission of droplets downstream (Gordillo et al., 2014). On the contrary, if the perturbations grow without bound, then the jet's free surface will break up next to the liquid source, leading to the so-called dripping mode.

The theoretical study of the steady jetting stability has been traditionally conducted also considering simple parts of the fluid domain, and applying a linear local analysis to them. An infinite cylindrical liquid jet (column) in vacuum is probably the simplest capillary system which one can think off. In this case, the study reduces to the temporal stability analysis to obtain the dispersion relationship, which allows one to calculate the continuum spectrum of eigenfrequencies characterizing the axisymmetric normal modes (Fourier components) as a function of their real wavenumbers (J. W. S. Rayleigh, 1892). The decomposition of initial perturbations into the corresponding eigenmodes has proved to be useful for studying the short-term evolution of those perturbations (García & González, 2008). The above conclusions do not apply to a semi-infinite

jet issuing from a nozzle. In this case, the spatial stability analysis constitutes a more realistic approach. The corresponding dispersion relation allows for the calculation of the (complex) wavenumber characterizing the perturbation evolution for a given (real) frequency (Leib & Goldstein, 1986a). The growth rates calculated in this way are in excellent agreement with experiments (González & García, 2009). Neither the temporal nor the spatial stability analyses of a liquid jet allow one to determine the parameter conditions for the steady jetting regime to occur when a liquid tapers from a source. For that purpose, one can conduct a spatio-temporal stability analysis (where both the wavenumber and frequency are complex numbers) to calculate the convective-to-absolute instability transition as a function of the governing parameters (Huerre & Monkewitz, 1990). It has been postulated that local convective instability throughout the whole fluid domain is sufficient to reach steady jetting. In this case, all the perturbations are convected downstream preserving both a stable liquid source and a steady filament long as compared to its diameter. On the contrary, absolute instability allows perturbations to travel upstream while growing, which is expected to cause either self-sustained oscillations or dripping. However, the link between absolute instability and these two phenomena is not clear even in relatively simple cases, where the base flow is almost uniform. For instance, (Yakubenko, 1997) has showed that inclined jets can suffer from self-sustained oscillations even if they are convectively unstable throughout the whole fluid domain. The Weber number for the convective-to-absolute instability transition significantly differs from that corresponding to the steady jetting instability in both plane liquid sheets (de Luca, 1999) and round jets (Dizes, 1997).

The main limitation of the spatio-temporal stability analysis is its local character, i.e., it is valid as long as the base flow explored by the perturbations is quasi-parallel and quasi-homogeneous in the streamwise direction. This approach has been successfully applied to slowly spatially developing (weakly non-parallel) base flows (Chomaz, 2005; Tammisola *et al.*, 2011). However, there are many applications where the hydrodynamic length characterizing the base flow is of the order of or even much smaller than that of the dominant perturbation, which invalidates the local approximation. In these cases, an accurate stability analysis requires the calculation of the global modes, which sheds new light in the physical mechanisms at play.

Global modes are patterns of motion depending in an inhomogeneous way on two or three spatial directions, and in which the entire system moves harmonically with the same (complex) frequency and a fixed phase relation (Theofilis, 2011). They are calculated as the eigenfunctions of the linearized Navier-Stokes operator as applied to a given configuration (base flow). If the spectrum of eigenvalues is in the stable complex half-plane, the base flow is linearly and *asymptotically* stable, which means that any initial small-amplitude perturbation will decay exponentially on time for $t \to \infty$ (as long as the linear approximation applies). Global instability is frequently linked to the convective-to-absolute instability transition, and is also assumed to cause either self-sustained oscillations or dripping. Tammisola, Lundell, and Soderberg (2011); Tammisola *et al.* (2012) have studied the effect of surface tension on the global stability of co-flow jets and wakes at a moderate Reynolds number. Sauter and Buggisch (2005) and Gordillo et al. (2014) have examined the global stability of jets stretched by the action of gravity and a coflowing stream, respectively.

Linear *asymptotic* global stability does not necessarily implies linear stability. If the linearized Navier-Stokes operator is normal, then the perturbation energy decreases monotonously not only in the asymptotic regime but also during the system's short-term response. On the contrary, if this last condition does not apply, there can be a transient growth of the perturbation energy before the asymptotic exponential regime is reached (Chomaz, 2005; Schmid, 2007). The short-term, non-exponential growth of small-amplitude perturbations can be responsible for the instability of asymptotically stable systems. In fact, convective instabilities commonly arising in problems with inflow and outflow conditions are not typically dominated by the long-term modal behavior. For instance, asymptotically stable gravitational jets eventually break up due to the growth of non-normal modes de Luca, Costa, and Caramiello (2002). Therefore, a base flow is stable according to linear asymptotic global stability only if (i) all the linear eigenmodes are stable, and (ii) the linearized Navier-Stokes operator associated with that flow is normal. If this last condition does not verify, more sophisticated approaches have to be taken to accurately capture the short-time dynamics, which may be more relevant to the overall flow physics.

Axisymmetric gaseous flow focusing (Gañán-Calvo, 1998) has be-

come a very popular technique to produce droplets in the steady jetting mode with diameters ranging from the sub-millimeter to the micrometer scale (Si et al., 2014; Trebbin et al., 2014; Forbes & Sisco, 2014). In this technique, a high-speed gas stream transfers energy to the liquid accumulated in a meniscus hanging on a feeding capillary through the collaborative action of both hydrostatic pressure and viscous shear forces. Flow focusing is attractive because produces jets much thinner than the discharge orifice, making use of purely hydrodynamic means, with no restrictions on the liquid properties.

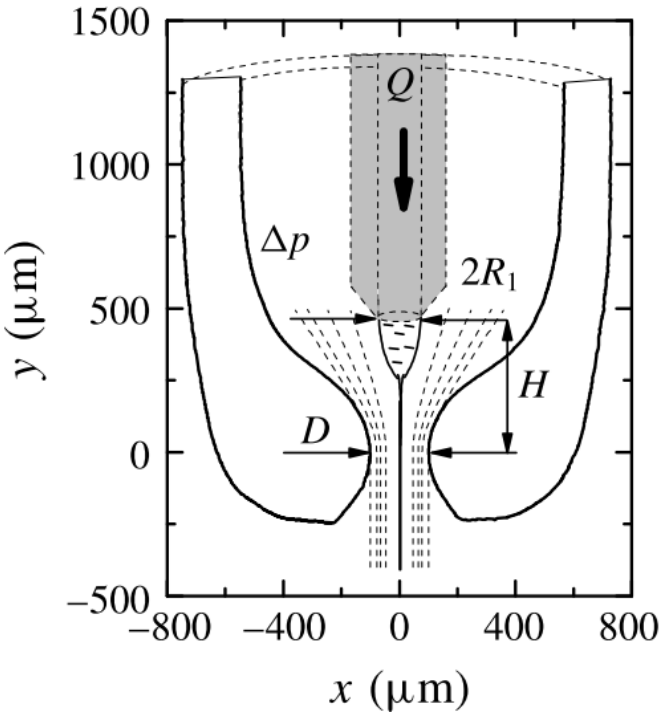

Figure 3.1: Sketch of the a convergent-divergent flow focusing nozzle used in the experimental study of Acero *et al.* (2012).

The minimum jet diameter in flow focusing is fundamentally determined by the axisymmetric instability arising when the injected liquid flow rate decreases below a certain threshold (Si et al., 2009; Vega et al., 2010; Montanero et al., 2011). This instability limit has been analyzed in terms of both the convective-to-absolute instability transition in

the emitted jet for low gas speeds, and the breakdown of the balance between viscosity, surface tension, and inertia in the liquid meniscus for sufficiently high gas velocities. The understanding of these two instability mechanisms has allowed us to rationalize the experimental results obtained both in the low- (Vega et al., 2010) and high-viscosity (Montanero et al., 2011) limits. However, there is not as yet a comprehensive study to describe the minimum flow rate instability on a rigorous basis. In this Chapter, we will conduct a linear global stability analysis of the base flow arising when a liquid meniscus is focused by a high-speed gaseous stream crossing a converging-diverging nozzle (Acero et al., 2012). We will calculate the axisymmetric eigenmodes, and determine the system's global stability limit as the parameter conditions for which the dominant mode becomes unstable. The comparison with experimental results will show that this analysis significantly underestimates the minimum flow rate for small enough gas speeds, which reveals the inability of the asymptotic stability theory to describing the short-term dynamics. This conclusion will be confirmed by direct numerical simulations of both the linearized and non-linear Navier-Stokes equations, which will show how perturbations introduced into globally stable base flows can grow over time. We will not consider the whipping instability because: (i) it strongly depends on the shape of the nozzle, which hinders the comparison between the numerical and experimental results; and (ii) the computing time for direct numerical simulations increases very significantly.

We consider an axisymmetric gaseous flow focusing configuration with a convergent-divergent gas aperture (see Fig. 3.1). A liquid of density ρ_ℓ and viscosity μ_ℓ is injected through a feeding capillary of diameter D_i at a constant flow rate Q_ℓ. The feeding capillary is located inside a converging-diverging nozzle with an orifice of diameter D. The distance between the capillary end and the nozzle neck is H. A gas stream of density ρ_g and viscosity μ_g flows through the nozzle driven by the applied pressure drop ΔP. An axisymmetric meniscus hangs on the edge of the capillary end due to the action of the surface tension σ. In the steady jetting regime, a liquid microjet tapers from the meniscus tip, and crosses the nozzle coflowing with the outer gas stream. The interfacial (capillary) sink of energy typically plays a secondary role as compared to the jet's kinetic energy (Gañán-Calvo, 1998). For this reason, the jet diameter downstream, D_j, essentially depends on the liquid density ρ_ℓ and viscosity μ_ℓ, as well as

on the control parameters Q_ℓ and ΔP. If one also neglects the viscous dissipation of energy, the conservation of this quantity yields (Gañán-Calvo, 1998)

$$D_j = D_j^{FF} \equiv \left(\frac{8\rho_\ell Q_\ell^2}{\pi^2 \Delta P} \right)^{1/4}. \tag{3.1}$$

This characteristic length allows us to bring up here the Reynolds and Weber numbers

$$\mathrm{Re}_\ell = \frac{\rho_\ell v_j^{FF} D_j^{FF}}{2\mu_\ell} \quad \text{and} \quad \mathrm{We}_\ell^{FF} = \frac{\rho_\ell (v_j^{FF})^2 D_j^{FF}}{2\sigma}, \tag{3.2}$$

where $v_j^{FF} \equiv 4Q_\ell/(\pi (D_j^{FF})^2$ is the mean velocity of the jet calculated from D_j^{FF}. The density and viscosity ratios, $\rho = \rho_g/\rho_\ell$ and $\mu = \mu_g/\mu_\ell$, take very small values in gaseous flow focusing, and thus their influence on the steady jetting stability can be neglected. For a fixed geometrical configuration, the three governing (dimensionless) parameters are Re_ℓ, We_ℓ and the Ohnesorge number $C = \mu_\ell (\rho_\ell \sigma R_1)^{-1/2}$.

Most of previous studies (Gañán-Calvo, 1998; Si et al., 2009; Vega et al., 2010; Acero et al., 2012) have examined the original flow focusing configuration (Gañán-Calvo, 1998) where the nozzle is replaced by a plate with an orifice. In these studies, the analysis has been simplified by examining the stability of the liquid source (meniscus) and the emitted jet separately: the steady jetting regime is assumed to be stable if and only if these two subdomains are stable. The liquid flow rate leading to the meniscus instability has been estimated through simple scaling analyses in both the inviscid (Vega et al., 2010) and viscous limits (Montanero et al., 2011). The jet's behavior has been described in terms of the spatio-temporal stability analysis for a uniform base flow (Leib & Goldstein, 1986a), which allows one to determine whether the jet is either convectively or absolutely unstable. Finally, for high enough liquid viscosities, the system runs into the surface tension barrier at the jet inception, $We_\ell \sim 1$ (Eggers & Villermaux, 2008), before the jet becomes absolutely unstable. Therefore, steady jetting gives rise to dripping if one of the above three instabilty limits is reached. Experimental results have shown that the first limit arises in the first place for large enough applied pressure drops (gas speeds) (Montanero et al., 2011), while either the second or third condition determines the steady jetting stability for sufficiently low values of ΔP (Si et al., 2009; Vega et al., 2010).

Experiments were conducted by Acero et al. (2012) to examine the stability of the steady jetting regime when focusing a liquid stream in a converging nozzle. For this purpose, the steady jetting was established for a sufficiently high liquid flow rate, and then the value of this quantity was progressively decreased while keeping the applied pressure drop constant. shows the projection of the experimental results onto the parameter plane defined by the Reynolds and Weber numbers (see Eq. 3.2) for different Ohnesorge numbers. The properties of the working liquids and the corresponding values of the Ohnesorge number are displayed in the following table.

Liquid	ρ (kg m^{-3})	σ (N m^{-1})	μ (Pa s)	C
500-cSt silicone oil	970	0.020	0.48	12.6
100-cSt silicone oil	961	0.021	0.096	2.47
5-cSt silicone oil	917	0.019	0.0046	0.127
Water	998	0.072	0.0010	0.0136

The steady jetting realizations also include those where the jet bends due to the whipping instability (not considered in this work). The jetting mode is limited by the existence of a minimum flow rate for large enough applied pressure drops (Vega et al., 2010; Acero et al., 2012). When this parameter takes small values, the behavior of the jet depends on the liquid viscosity: the convective-to-absolute instability transition becomes dominant for low and moderate viscosities (water and 5-cSt silicone oil) (Vega et al., 2010), while the instability barrier $\mathrm{We}_\ell \simeq 1$ is reached in the high-viscosity cases (100-cSt and 500-cSt silicone oils) before the jet becomes absolutely unstable (Acero et al., 2012).

As can be seen, the stability analysis of axisymmetric flow focusing is a compendium of several rules which must be applied in a different way depending on the properties of the focused liquids. In particular, the local stability analysis of the emitted jet does not predict the existence of a minimum flow rate for large applied pressure drops, which is the most relevant stability limit at the technological level. Therefore, a comprehensive and more rigurous stability study of the present fluid configuration is desirable. This study demands the calculation of the linear global modes.

3.2 Numerical modeling

Bulk and interface equations - In this section, all the variables are made dimensionless with the capillary radius R_1, the liquid density ρ_ℓ, and the surface tension σ, which yields the characteristic time and velocity scales $t_c = (\rho_\ell D_i^3/8\sigma)^{1/2}$ and $v_c = D_i/2t_c$, respectively. The dimensionless, axisymmetric, incompressible Navier-Stokes equations for the velocity $\mathbf{v}^{(j)}(r,z;t)$ and pressure $p^{(j)}(r,z;t)$ fields are

$$\nabla \cdot \mathbf{v}^{(j)} = 0, \tag{3.3}$$

$$\frac{\partial \mathbf{v}^{(j)}}{\partial t} + \rho^{\delta_{jg}}(\mathbf{v}^{(j)} \cdot \nabla)\mathbf{v}^{(j)} = -\nabla p^{(j)} + \mu^{\delta_{jg}} C \nabla^2 \mathbf{v}^{(j)}, \tag{3.4}$$

where t is the time, r (z) is the radial (axial) coordinate, $u^{(j)}$ ($w^{(j)}$) is the radial (axial) velocity component, and δ_{ij} is the Kronecker delta. In the above equations and henceforth, the superscripts $j = \ell$ and g refer to the liquid and gas phases, respectively, while the subscripts t, r, and z denote the partial derivatives with respect to the corresponding variables. The action of the gravitational field has been neglected due to the smallness of the fluid configuration.

Taking into account the kinematic compatibility and equilibrium of tangential and normal stresses at the interface $r = F(z,t)$, one gets the following equations:

$$F_z w^{(\ell)} - u^{(\ell)} = F_z w^{(g)} - u^{(g)} = 0, \tag{3.5}$$

$$\begin{aligned}&(1-F_z^2)(w_r^{(\ell)} + u_z^{(\ell)}) + 2F_z(u_r^{(\ell)} - w_z^{(\ell)}) = \\ &\mu[(1-F_z^2)(w_r^{(g)} + u_z^{(g)}) + 2F_z(u_r^{(g)} - w_z^{(g)})]\end{aligned} \tag{3.6}$$

$$\begin{aligned}&p^{(\ell)} + \frac{FF_{zz} - 1 - F_z^2}{F(1+F_z^2)^{3/2}} - \frac{2C[u_r^{(\ell)} - F_z(w_r^{(\ell)} + u_z^{(\ell)}) + F_z^2 w_z^{(\ell)}]}{1+F_z^2} = \\ &p^{(g)} - \frac{2\mu C[u_r^{(g)} - F_z(w_r^{(g)} + u_z^{(g)}) + F_z^2 w_z^{(g)}]}{1+F_z^2}.\end{aligned} \tag{3.7}$$

Boundary conditions and geometry - The Navier-Stokes equations are integrated in the numerical domain sketched (see Fig. 3.2). The (dimensionless) shape $S(z)$ of the nozzle is given by the function

$$S(z) = \begin{cases} R_{ml} - a_l \tanh[\alpha_l (z - z_{ml})] & \text{for} \quad 0 \le z \le L_l \\ R_{mr} + a_r \tanh[\alpha_r (z - z_{mr})] & \text{for} \quad L_l < z \le L_l + L_r \end{cases}, \tag{3.8}$$

where $R_{ml,r} = (R_{l,r} + D/2)/2$ and $a_{l,r} = (R_{l,r} - D/2)/2$. The shape of the converging part of the nozzle is given by the parameters R_l, D, and α_l, while its position in our coordinate system and length are determined from z_{ml} and L_l, respectively. Analogously, the shape of the diverging part of the nozzle is defined by the parameters R_r, D, and α_r, while its length is L_r. The mid-point axial position of the diverging part, z_{mr}, is calculated from the continuity condition of $S(z)$ at $z = L_l$. Finally, the parameter H characterizes the axial position of the feeding capillary end in the nozzle. In our simulations, $R_l = 2.67$, $R_r = 5.33$, $D = 2.59$, $\alpha_l = \alpha_r = 1$, $z_{ml} = 6.93$, $L_l = L_r = 10$, and $H = 5.87$.

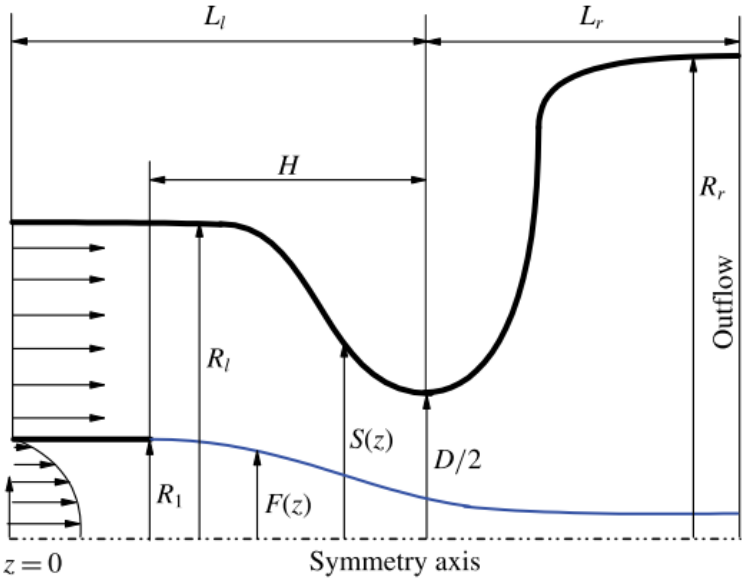

Figure 3.2: Sketch of the computational domain of the convergent-divergent nozzle.

At the inlet section $z = 0$, we impose an uniform velocity profile in the gaseous stream, and the Hagen-Poiseuille velocity distribution $u^{(\ell)} = 0$

and $w^{(\ell)} = 2v_e(1-r^2)$ ($v_e = 4Q_\ell/(\pi D_i^2 v_c)$) in the liquid domain. The gas inlet velocity is adjusted so that the pressure drop ΔP between the inlet and outlet sections of the numerical domain corresponds to that of the experiments. The non-slip boundary condition is imposed at the solid walls. We prescribe the standard regularity conditions $u^{(\ell)} = w_r^{(\ell)} = 0$ at the symmetry axis, and the outflow conditions $u_z^{(j)} = w_z^{(j)} = F_z = 0$ at the right-hand end $z = L_l + L_r$ of the computational domain. We verified that the results are not significantly affected by this last condition by comparing the stability limits for different values of L_r.

Numerical method - The hydrodynamic equations are spatially discretized with the Chebyshev spectral collocation technique using 35 and 1001 collocation points along the radial and axial directions, respectively. We conducted simulations for different mesh sizes to ensure that the results did not depend on that choice It is important to note that a coordinate transformation is required for mapping the physical fluid domain of (r,z) onto square computational domains in mapped coordinates (ξ,η). In the liquid phase, the mapped radial and longitudinal coordinates turns out $\xi_\ell = r/F(z,t)$, $\eta_\ell = z/(L_l+L_r)$, respectively. In the gas phase, the transformations are $\xi_g = (r-F(z,t))/(S(z)-F(z,t))$ and $\eta_g = z/(L_l+L_r)$. Note that $\xi_\ell, \xi_g, \eta_\ell, \eta_g \in [0,1]$. To calculate the linear global modes, one assumes the temporal dependence $U(r,z;t) = U_0(r,z) + \varepsilon \delta U(r,z)\, e^{-i\omega t}$ ($\varepsilon \ll 1$). Here, $U(r,z;t)$ represents any hydrodynamic quantity, $U_0(r,z)$ and $\delta U(r,z)$ stand for the base (steady) solution and the spatial dependence of the eigenmode, respectively, while $\omega = \omega_r + i\omega_i$ is the eigenfrequency. Both the eigenfrequencies ω and the corresponding eigenmodes δU are calculated as a function of the governing parameters. The dominant eigenmode is that with the largest growth factor ω_i. If that growth factor is positive, the base flow is asymptotically unstable (Theofilis, 2011). In the direct numerical simulations, the time-dependent fluid region is mapped onto a fixed numerical domain through a coordinate transformation. An implicit time advancement is performed using second-order backward finite differences. For the interested reader, further details about the numerical procedure can be found in (Herrada & Montanero, 2016), where it is shown how the the method for solving the eigenvalue and time-dependent problems are essentially the same. Here, we will give a brief note. The elements of the Jacobian $\mathscr{J}^{(p,q)}$ for the discretized equations

have to fulfill $\mathscr{J}^{(p,q)}U_o^{(q)} = \mathscr{F}^{(p)}$given the unknowns from the base flow U_o^q ($q = 1,2,...,n \times N$ are the n unknowns evaluated at the N grid points). Previous relations are computed by symbolic algorithm using standard software available in the market. For the iterative Newton-Raphson process, those functions have to be simply evaluated numerically for each step, which reduces the computational costs. The updating vector is obtained as $\delta U_o^{(q)} = -\mathscr{J}^{(p,q)}\mathscr{F}^{(p)}$, where the functions $\mathscr{F}^{(p)}$ come from the evaluation at each spatial point for the previous iteration. Due to the analogy of both problems, the briefly commented procedure can be used for the determination of the eigenvalue problem linked to the linear global modes of the system. The spatial dependence of the linear perturbation $\delta U^{(q)}$ is the solution to the generalized eigenvalue problem $\mathscr{J}_o^{(p,q)}\delta U^{(q)} = i\omega\mathscr{Q}_o^{(p,q)}\delta U^{(q)}$, where $\mathscr{J}_o^{(p,q)}$ is the Jacobian of the system evaluated with the base solution $U_o^{(q)}$, and $\mathscr{Q}_o^{(p,q)}$ accounts for the temporal dependence of the problem. Therefore, the numerical algorithm developed for the base flow problem can also be applied to the linear stability analysis.

Base flow and spectrum - Figures 3.3 and 3.4 (top) show two stable base flows calculated for the lowest and highest Ohnesorge numbers considered in this work. In the low-Ohnesorge number case, the viscous shear stress exerted by the high-speed gas stream over the free surface accelerates the liquid there, and drags it towards the meniscus tip. The pressure increases at the stagnation point located right in front of the emitted jet, which pushes the liquid backwards across the meniscus. The resulting recirculation cell occupies the entire meniscus and enters the feeding capillary. In the high-Ohnesorge number case, the gas current does not form the recirculation cell due to the strong viscous stresses arising in the liquid meniscus. Those stresses arrange the streamlines and direct the flow in the meniscus tip. The resulting flow pattern becomes similar to that appearing in liquid-liquid coflowing configurations. Figures 3.3 and 3.4 (bottom) show the spectrum of eigenvalues $\omega = \omega_r + i\omega_i$ with oscillation frequencies ω_r around that of the dominant mode. The open symbols are the eigenvalues characterizing the linear global modes of the stable base flows in figures 3.3, 3.4, while the solid symbols correspond to those obtained when the liquid flow rate is slightly decreased while keeping the applied pressure drop constant until those flows become asymptotically

unstable.

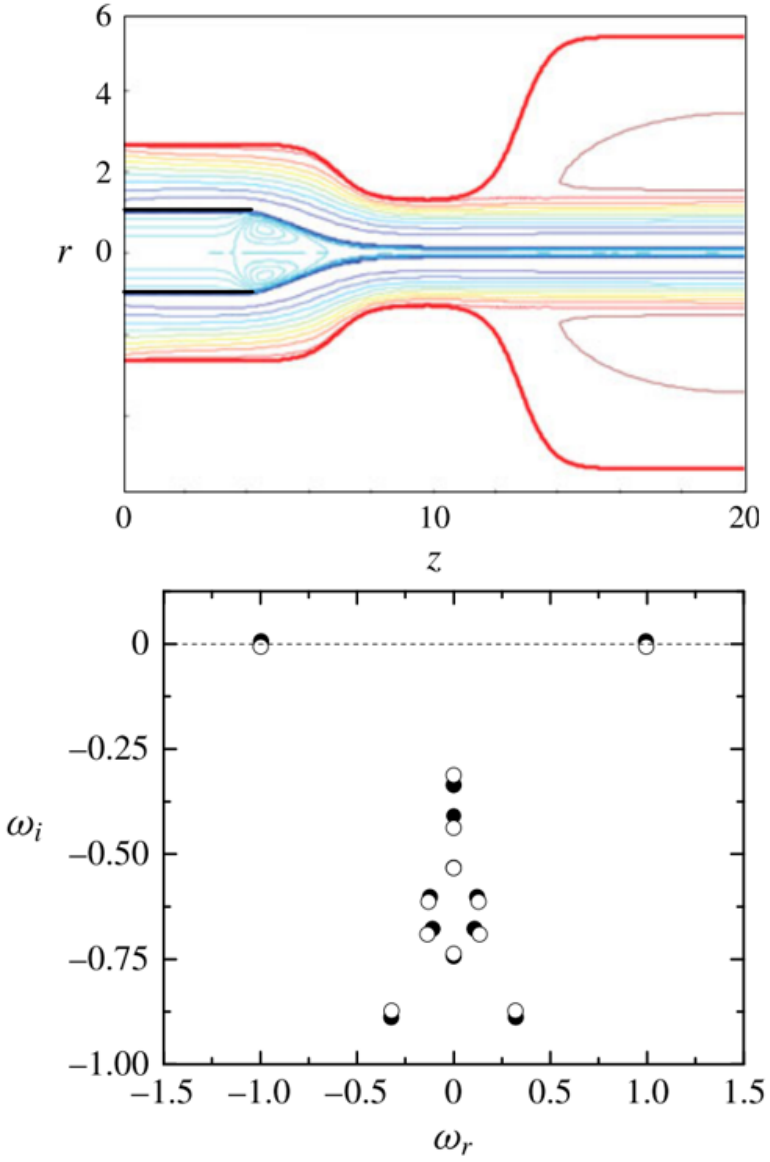

Figure 3.3: Marginally stable conditions of the base flow (top) for $Re_\ell = 34.3$, $We_\ell = 2.03$ and $C = 0.0136$ together with the eigenvalues (bottom) for the latter conditions (open symbols) and also for $Re_\ell = 33.6$, $We_\ell = 1.98$ and $C = 0.0136$ (solid symbols).

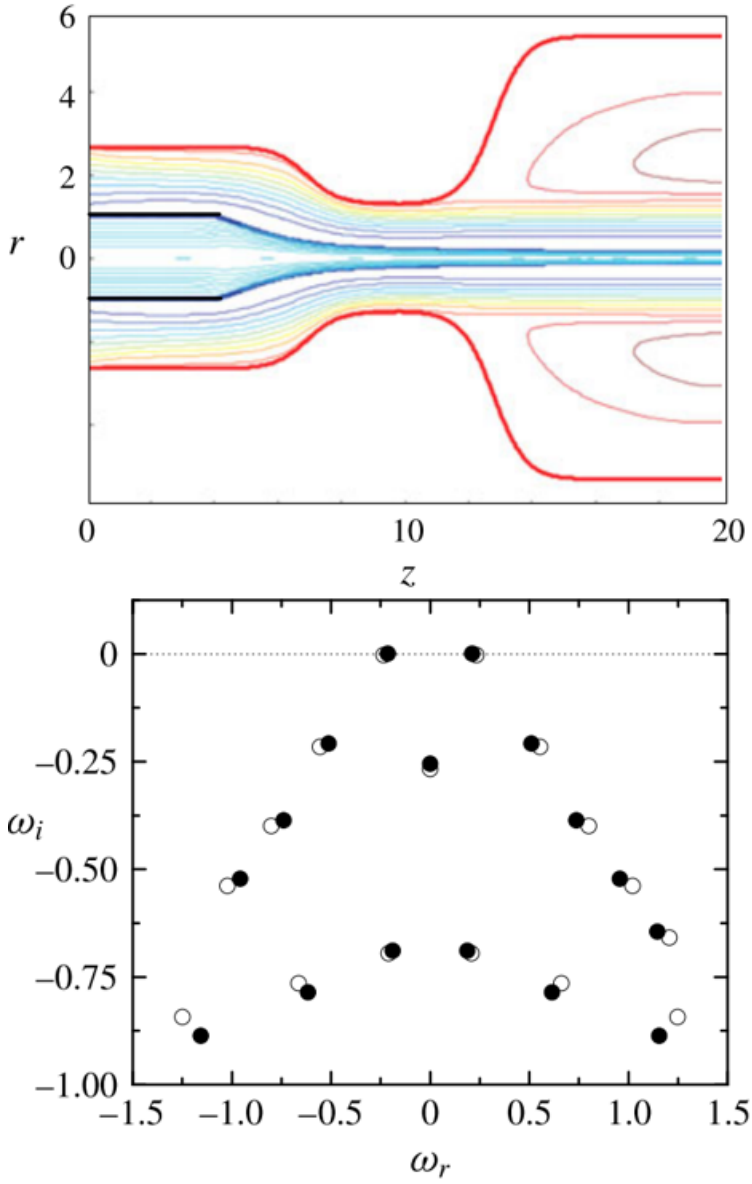

Figure 3.4: Marginally stable conditions of the base flow (top) for $Re_\ell = 0.045$, $We_\ell = 2.27$ and $C = 12.6$ together with the eigenvalues (bottom) for the latter conditions (open symbols) and also for $Re_\ell = 0.0421$, $We_\ell = 2.12$ and $C = 12.6$ (solid symbols)

The point representing the dominant global mode slightly moves up,

and crosses the complex plane imaginary axis causing asymptotic instability. The frequency of this mode is around unity for the low-viscosity liquid. This means that the flow focusing steady regime becomes asymptotically unstable due to the unbounded growth of self-excited oscillations characterized by a frequency that approximately equals the inverse of the capillary time. The frequency of the dominant mode considerably decreases as viscosity increases, while the opposite occurs to the subdominant ones.

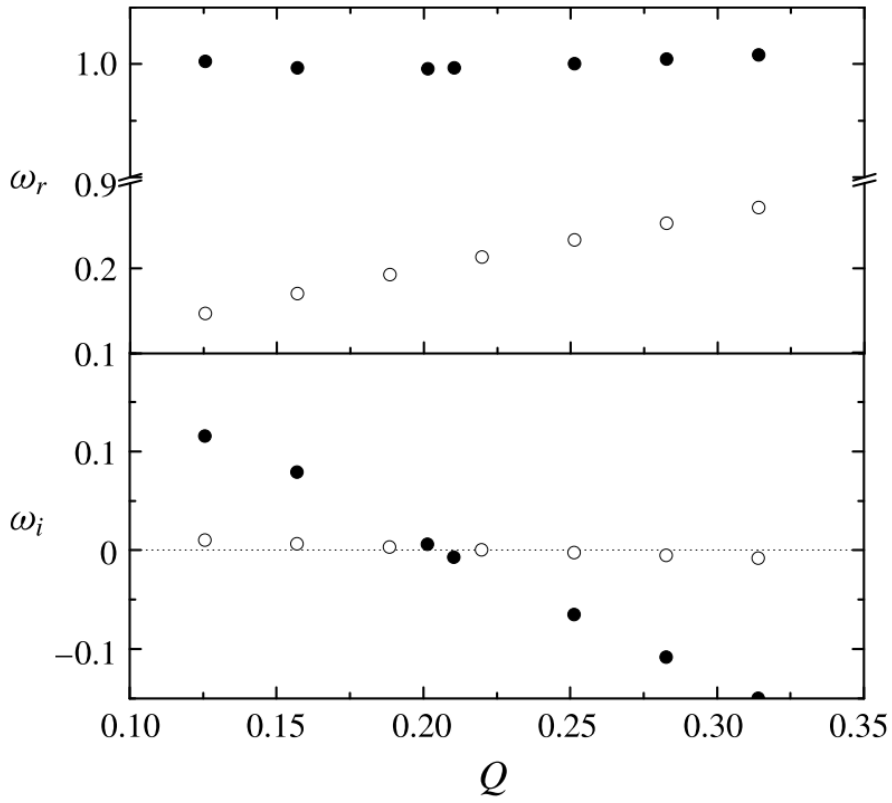

Figure 3.5: Oscillation frequency ω_r and growth factor ω_i as a function of the liquid flow rate Q_ℓ for $\Delta p = 7.78$. The solid and open symbols correspond to $C = 0.0136$ and 12.6, respectively.

Sensibility of (ω_i, ω_r) *with* Q_ℓ - Figure 3.5 shows the evolution of the dominant eigenvalue as the liquid flow rate decreases for a constant applied pressure drop. This figure illustrates what happens in a typical flow

flow focusing experiment, when the stability limit is determined starting from a stable configuration for a sufficiently large flow rate, and then this quantity is progressively decreased while keeping the applied pressure constant (Acero et al., 2012). The oscillation frequency ω_r of the dominant mode is practically independent of the liquid flow rate in the low-viscosity case, while it significantly decreases as Q_ℓ decreases for the viscous liquid. The growth rate exhibits a quasi-linear dependence with respect to the liquid flow rate in both the low- and high-viscosity cases. The slope of the curve $\omega_i(Q_\ell)$ for the viscous liquid is much smaller than in the low-viscosity case, which suggests that the minimum flow rate is more sensitive to variations of the rest of governing parameters in the former case. The minimum flow rate is around $0.2(\sigma D_i^3/8\rho_\ell)^{1/2}$ for both water and 500-cSt silicone oil. Because the water surface tension is much larger than that of 500-cSt silicone oil, the above result implies that the minimum flow rate is considerably smaller in the latter case, in agreement with previous experimental observations (Acero et al., 2012).

Experimental validation - The stability limits corresponding to the jetting-to-dripping transition in (Acero et al., 2012) are compared with the corresponding predictions obtained from the asymptotic global stability analysis (see Fig.3.6). There is remarkable agreement between the experimental and theoretical results for 5-cSt and 100-cSt silicone oils. The linear stability analysis satisfactorily captures the influence of viscosity in all the cases. The theoretical predictions for water systematically underestimate the critical flow rate for Weber numbers larger than unity (large applied pressure drops), which leads to a stable parameter region bigger than that observed in the experiments. This pancy can be explained in terms of the finite-amplitude perturbations that inevitably appear in experiments, which can destabilize configurations stable under infinitesimal disturbances. The pressure waves driven by the syringe pump used to inject the liquid constitutes an example of such perturbations (Korczyk *et al.*, 2011). The theoretical predictions for 500-cSt silicone oil systematically overestimate the minimum flow rate for Weber numbers larger than unity. This means that steady jetting realizations were observed in the experiments even for asymptotically unstable configurations. This discrepancy cannot be attributed to possibly stabilizing effects of non-linear terms, which would yield self-sustained oscillations not observed in the experiments. A plausible explanation for this deviation may be found in

the differences between the numerical and experimental geometries. On one side, the nozzle inner shape was modeled in the simulations by the function (3.8) to simplify the numerical calculations. On the other side, the experiments were conducted for a large ratio H/D (close to its maximum possible value), and therefore small variations of the capillary position H must considerably influence the critical flow rate, according to the experimental data of Montanero et al. (2011) for the plate-orifice configuration.

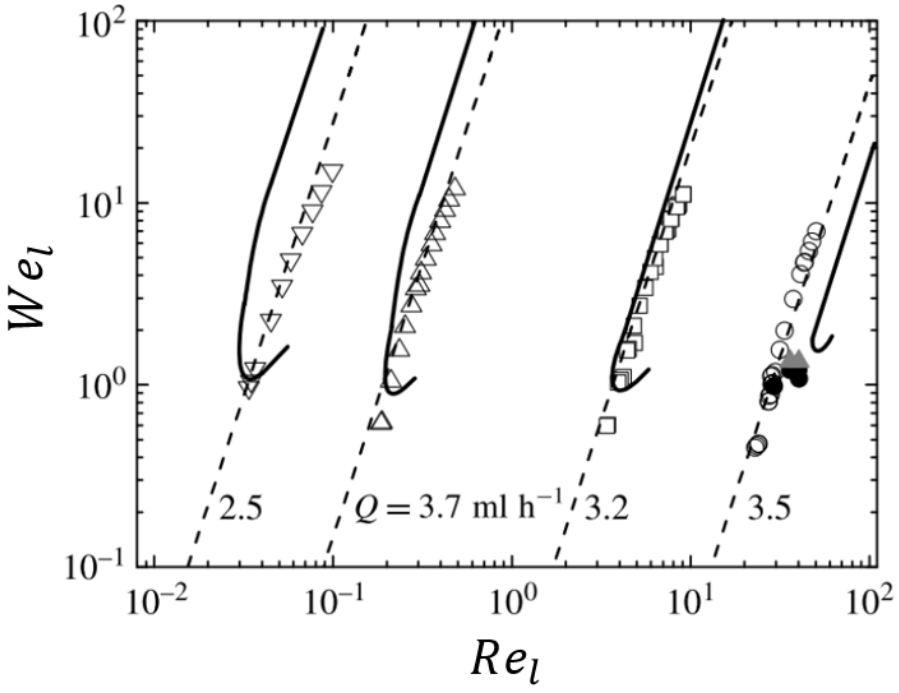

Figure 3.6: Stability map for the flow focusing configuration shown in figure 2. From right to left, the solid lines approximately correspond to the experimental jetting-to-dripping transitions shown in (Acero *et al.*, 2012) for C = 0.0136 (water), 0.127 (5-cSt silicone oil), 2.47 (100-cSt silicone oil) and 12.6 (500-cSt silicone oil), respectively. The open symbols are the corresponding transitions from asymptotically stable-to-unstable base flows. The figure shows the minimum flow rates estimated from these theoretical predictions. The solid triangles and circles are stable and unstable direct numerical simulations for water, respectively.

These geometrical deviations are expected to affect the minimum flow rate to a greater extent for high viscosities because of the large sensitivity of that threshold to small variations of the rest of parameters in that case (see Fig. 3.5). Confirming the validity of this explanation would require a systematic parameter study that is beyond the scope of the present thesis. The asymptotic stability limit curves do not have the elbow observed in the experiments for Weber numbers around unity. In the next subsection, we will explain this discrepancy in terms of a convective instability resulting from the superposition at short times of asymptotically stable global modes. For this purpose, the Navier-Stokes equations will be integrated over time to monitor the evolution of small perturbations introduced into the liquid meniscus. It must be noted that previous studies (Si et al., 2009; Montanero et al., 2011) have already recognized that the nature of this instability is different from that arising for large pressure drops (Weber numbers). In fact, they have described the phenomenon in terms of the convective-to-absolute instability transition (Huerre & Monkewitz, 1990) taking place in an infinite cylindrical jet.

Energy of the perturbation- In order to gain insight into the physical mechanisms responsible for the asymptotic global instability, we consider the kinetic energy $e \equiv p + 1/2\,\rho^{\delta_{jg}}\,(|u^{(j)}|^2 + |w^{(j)}|^2)$ associated with the eigenmode. Figures 3.7 a,b, shows the isolines of this quantity for the modes causing the instability of the base flows in figures 3.3 and 3.4 (top). The scalar fields $e(r,z)$ in the liquid and gas domains have been normalized with their corresponding maximum values. The maximum values in the liquid domain are around 132 and 37 times as those of the gas stream for the low- and high-viscosity cases, respectively. This indicates that the physical origin of the instability must be located in the liquid domain, as assumed in previous studies (Si et al., 2009; Montanero et al., 2011; Acero et al., 2012). The perturbation energy in the liquid domain increases monotonously along the streamwise direction. The perturbation energy of the gas increases both next to the jet's free surface and in the shear layers between the gas current and the outer recirculation cells.

Short-term response - In this subsection, we analyze the temporal evolution of a small perturbation introduced into an asymptotically stable base flow. The perturbation consists in the deformation of the free surface (the velocity and pressure fields are not perturbed) at $t = 0$ given by the Dirac

delta function

$$\widehat{f}(z) = \beta \; e^{-(z-z_0)^2/a^2} \; , \tag{3.9}$$

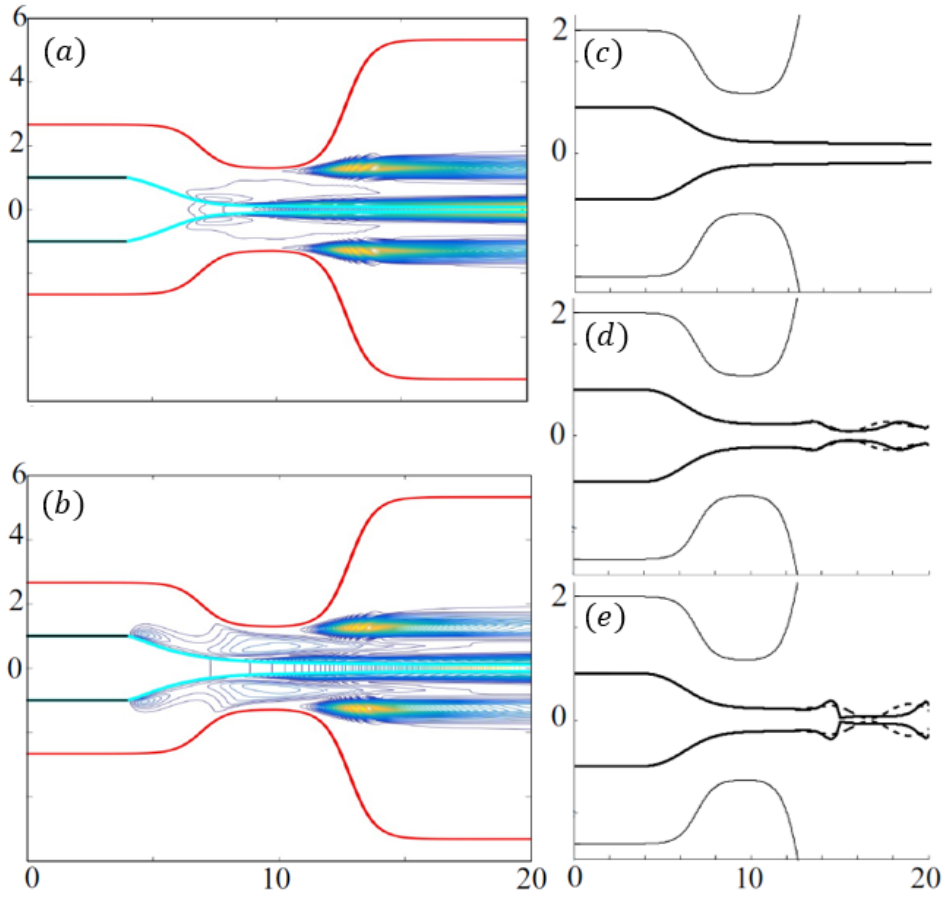

Figure 3.7: Perturbation energy e for $Re_\ell = 33.6$, $We_\ell = 1.98$ and $C = 0.0136$ (a), and for $Re_\ell = 0.0421$, $We_\ell = 2.12$ and $C = 12.6$ (b). The scalar fields $e(r,z)$ in the liquid and gas domains have been normalized with their corresponding maximum values. The maximum values in the liquid domain are approximately 132 and 37 times as those of the gas stream for the low- and high-viscosity cases, respectively. Higher (lower) values of e correspond to the colour yellow (blue). Free-surface deformation calculated with the linearized (dash line) and nonlinear (solid line) hydrodynamic equations at t = 0 (c), 4 (d) and 4.3 (e) for $Re_\ell = 40.1$, $We_\ell = 1.21$ and $C = 0.0136$.

where β indicates the maximum deformation, while z_0 and a are the impulse location and width, respectively. In all the cases, a small-amplitude ($\beta = 0.01$) deformation is introduced in the liquid meniscus ($z_0 = 4.5$) with a width ($a = 0.1$) sufficiently small for the impulse to trigger a train of capillary waves with a wide range of wavelengths.

We have integrated the Navier-Stokes equations and boundary conditions linearized around the base flow to examine its short-term response to the impulse with the same governing equations as those of the asymptotic global stability analysis. Figures 3.7 c,d,e show the free surface deformation at three instants for an asymptotically stable base flow. Due to the small magnitude of the perturbation, the free surface deformation is hardly noticeable at $t = 0$. Owing to the non-normal character of the linearized Navier-Stokes operator, the superposition of decaying perturbations triggered by Eq. 3.9 gives rise to the free surface pinch-off within the numerical domain. This kind of short-term convective instability does not cause oscillations of the liquid meniscus, as also shown by the experiments (Si et al., 2009; Vega et al., 2010).

In the dripping mode of flow focusing, the liquid free surface breaks up at distances from the discharge orifice of the order of its diameter. Therefore, it is reasonable to identify as dripping those simulations where the free surface pinches within our numerical domain, and as jetting otherwise. The solid circles (triangles) in Fig.3.6 correspond to dripping (jetting) flow focusing realizations for water. As can be observed, the short-term convective instability explains the elbow of the stability limit curve for Weber numbers around unity, i.e., why steady jetting becomes unstable and evolves towards dripping for Weber numbers less than unity even if the flow rate is larger than the critical value predicted by the asymptotic stability analysis.

Figures 3.7 c,d,e also show the free surface deformation when the non-linear terms of the hydrodynamic equations are taken into account. As can be observed, these terms do not manage to stabilize the perturbation, and the jet's free surface breaks up next to the liquid source (dripping mode). As expected, only the free-surface pinch-off is affected by non-linearities, while the latter remain inconsequential in the rest of the numerical domain. Naturally, there is a small jet portion next to the outlet section "contaminated" by the outflow boundary condition (especially in the non-linear simulation), but this defficiency does not affect the validity of the

above conclusions. Modal stability theory lies in the assumption that the linearized Navier-Stokes operator is normal, which guaranties that the energy of small-amplitude perturbations around asymptotically stable base flows decreases monotonously both during the short-term response and the asymptotic regime. However, there can be situations where that condition does not verify (Chomaz, 2005; Schmid, 2007). In this case, asymptotic global stability is a necessary but not sufficient condition for stability.

The present study provides a comprehensive understanding of the flow focusing stability problem, improving previous partial explanations based on local stability analysis (Huerre & Monkewitz, 1990; Eggers & Villermaux, 2008; Si et al., 2009; Montanero et al., 2011) and scaling laws (Vega et al., 2010; Montanero et al., 2011; Acero et al., 2012). The analysis can extended to a number of similar microfluidic configurations, including coflow systems, electrospray, liquid-liquid flow focusing. In this sense, we will include electrohydrodynamic fields together with gaseous streams in the next chapter.

3.3 Jet speed maximization for MHz-SFX

During 2007, we had the opportunity to participate in an experiment at FLASH (DESY, Germany) (Wiedorn et al, 2018), where strongly miniaturized ceramic flow focusing nozzle was used for showing its potential as fast delivery method of molecules at megahertz XFEL experiments, particularly at much harder XFEL sources like European XFEL. Indeed, jet speed almost reached 80 m/s, avoiding the issues from gap dynamics. The Ph. D. candidate contributed in this work with the test and preparation of nozzles during the beamtime and later on with theoretical discussions.

Some months later, we report the significant role played by gas-focused liquid jets in the first experiments that took place in September 2017 and April 2018 at the European XFEL, particularly at their SPB/SFX instrument. Those experiments were performed according to the proposal XFEL2012, led by Prof. H. N. Chapman and Dr. A. Barty.

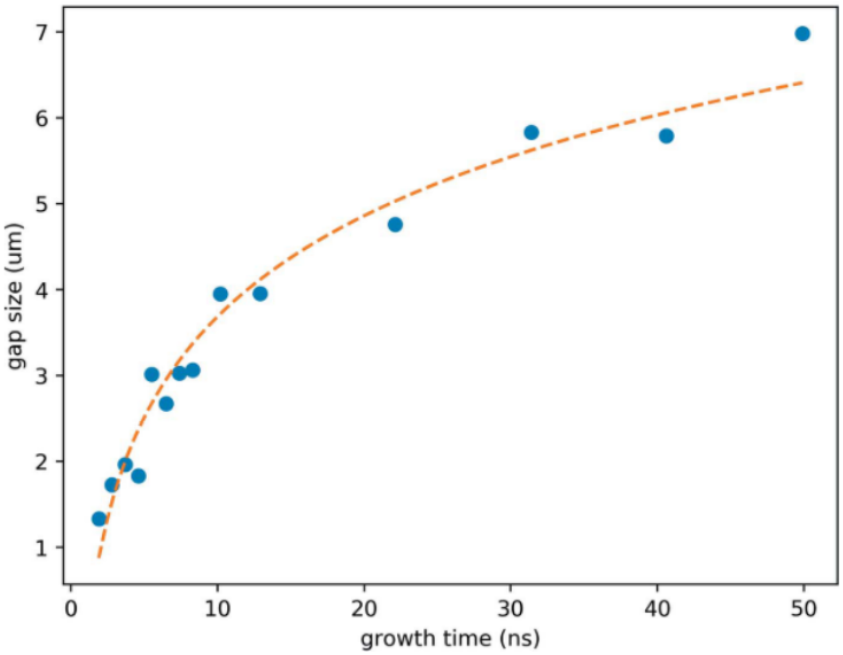

Figure 3.8: Plot of the evolution of the gap size in the first 50 ns after the FLASH FEL pulse hit the jet (solid circles) and the fit of a logarithmic function to the data (dashed line). The jet was flowing at a rate of 6.7 mL/min (helium mass-flow rate $Q_{mg} = 2.6$ mg/min) with a diameter $D_j =$ 3.1 mm and velocity $v_j = 60$ m/s. The dose deposited into the jet was approximately 30 MGy. Note that the position of the gap in the jet varies as a result of nozzle vibrations (Wiedorn et al, 2018).

Besides theoretical discussions, the participation of the Ph. D. candidate consisted in the preparation, assembly and test of flow focusing nozzles used at the beamline. Here, we briefly sum up the main results of the work based on those experiments (Wiedorn *et al.*, 2018).

Fast jets - As we said above, the delivery of crystal suspensions was carried out through gas-focused liquid jets. The fluid setup was formed by a high-pressure liquid chromatography (HPLC) pump (Shimadzu) for an accurate control of the steadiness of the liquid flow rate Q_ℓ injected. Given that interesting values for Q_ℓ should be around the minimum liquid flow rate attainable $Q_{\ell min}$, keeping a steady flow rate turns out essential.

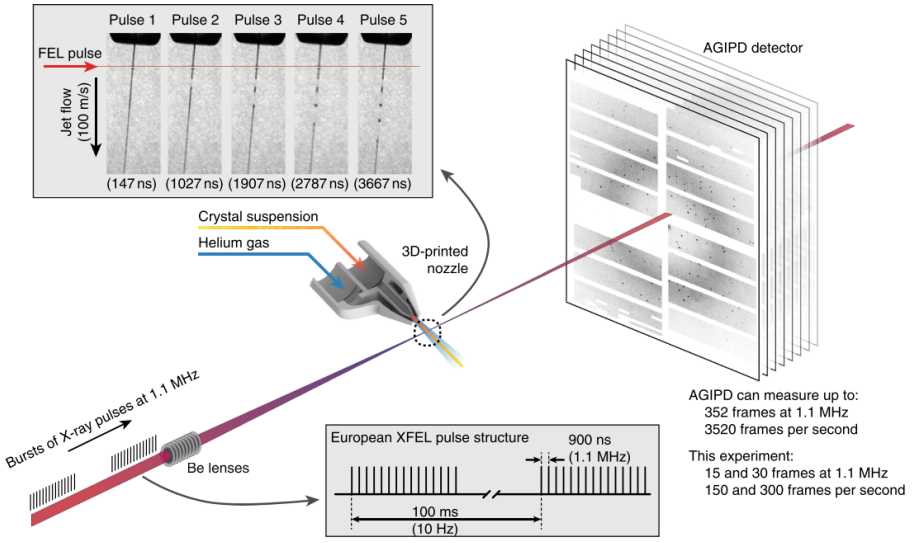

Figure 3.9: Megahertz serial crystallography. Pulses from the European XFEL were focused on the interaction region using a set of Beryllium lenses. Protein crystals in crystallization solution were introduced into the focused XFEL beam using a liquid jet of 1.8 μm diameter moving at speeds between 50 m/s and 100 m/s. Diffraction from the sample was measured using an AGIPD, which is capable of measuring up to 3520 pulses per second at megahertz frame rates. In−situ jet imaging (inset) showed that the liquid column does explode under the X−ray illumination conditions of this experiment using a jet with a speed of 100 m/s, but that the liquid jet recovered in less than 1 μs to deliver fresh sample in time for arrival of the next X-ray pulse. Images and movies of jets at different speeds are included in the supplementary material. (Wiedorn et al, 2018).

As gas stream, Helium was the chosen one. Its use not only comes from the low electronic interaction of a monovalent element as Helium, but also for its low density ($\rho_{He(g)} = 0.164$ kg/m^3). Both liquid and gas flows were monitored by a liquid flow meter (Sensirion) and a gas flow meter (Bronkhorst), respectively. Likewise, the pressure of the gas stream was commanded by the use of a pressure regulator (Proportion-air). On the other hand, nozzle tips were designed for tiny inner diameters ($D_i = 50$ μm) together with even smaller gaseous apertures ($D_g = 30$ μm) (see Fig.). They were fabricated by a high-resolution 3D printing (Nanoscribe,

GmbH) by using a similar strategy already proposed by Nesdag. Input lines of both sample and gas were fused silica tubes with internal diameters of 50 μm and 100-200 μm, respectively. With this strong nozzle miniaturization, we could reach steady jetting conditions with suitable jet speeds, randing from 50 to 100 m/s.

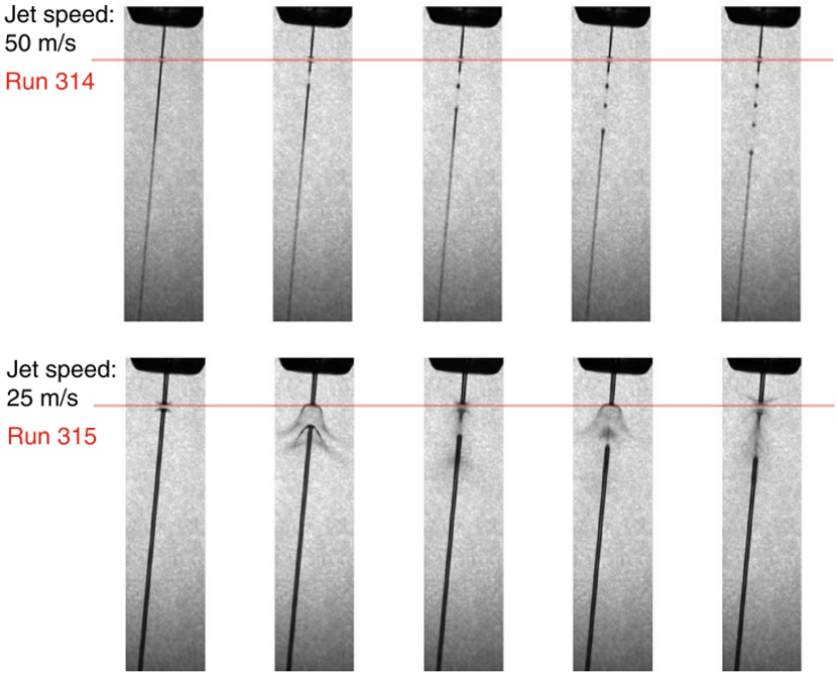

Figure 3.10: Images of interaction of the EuXFEL liquid jet for the first 5 pulses in a train. Jets over 50 m/s (top row) recover in time for the next pulse, whereas slower jets of the type commonly used at LCLS do not recover in time for the next XFEL pulse at MHz repetition rates (bottom row). Red line shows the intersection point with X-ray pulses. Images obtained by synchronized laser back illumination. (Wiedorn et al, 2018).

XFEL conditions will be described in the following the lines. Optical imaging of single shots provided data for an estimates of the focal spot ($D_B \sim 16$ μm) at the interaction region between the XFEL pulse and the liquid jet. Note that the aspect ratio between focal spot and jet diameter could induce a different typology of explosions. In particular, the pulse structure of this experiment was 30 pulses per burst at 1.1 MHz repetition

rate, with a burst rate of 10 Hz. It must be noted that a performance of European XFEL at full capabilities should comply with design parameters in a near future (i.e., 2700 pulses at 4.5 MHz, with a burst rate of 10 Hz).

Chapter 4

Electrified liquid jets assisted by co-flowing gas streams

> Although the mills of God
> grind slowly, yet they grind
> exceeding small
>
> Friedrich von Logau

Electrospray has been extensively used for producing highly focused liquid cone-jets in a great amount of scientific applications and technological industries. However, the extreme requirements imposed by SFX experiments and their prospects makes crucial the optimization of the liquid injection. So, in this chapter, we introduce a novel way of improving the stability of electrified jets by the action of co-flowing gas streams. For a given liquid, our method enables to generate steady jets with smaller diameters and bigger speeds than electrospray alone can reach by itself. Besides, we derive the scaling laws behind the dripping-jetting transition for cone-jets as a function of the governing parameters involved. We validate this insight through experimental realizations and a global stability analysis of the configuration. Besides, we check configuration theoretically through a global stability analysis as a function of the governing parameters involved. Additionally, we performed a set of experiments to verify what parameters influence the jet length. We adopt a very recent model for capillary jet length to our configuration by com-

bining electrohydrodynamic effects with the gas flow through an equivalent liquid pressure. Due to the diameters below 1 micrometer and high speeds attainable in excess of 100 m/s, this concept has the potential to be utilized for structural biology analyses with X-ray free-electron lasers at megahertz repetition rates as well as other applications.

4.1 Optimization of steady cone-jets

The ubiquitous study of liquid jets and drops during the last decades (Eggers & Villermaux, 2008) has accompanied their increasing use in applications within analytical chemistry (Fenn et al., 1989), (Takáts et al., 2004) or material science (Jaworek, 2007) among others. In this sense, a prominent example is *Serial Femtosecond Crystallography* (SFX) (Chapman *et al.*, 2011), with the use of flow focusing (FF) (Gañán-Calvo, 1998), (DePonte et al., 2008), (Oberthür *et al.*, 2017) and electrospray (ES) (Sierra *et al.*, 2012), (Sierra *et al.*, 2015) for carrying biological samples to the region where they interact with the focused X-ray pulse (Pellegrini et al., 2016), (Neutze et al., 2000). With the introduction of X-ray free-electron laser facilities that produce pulses at megahertz rates, even smaller and faster liquids are required (Wiedorn *et al.*, 2018). The interaction with each X-pulse is quite violent and influences more than just the intersecting volume of the X-ray beam with the jet. The jets need to run fast enough to introduce fresh sample on each pulse, taking into account the explosive interaction with the X-rays (Stan *et al.*, 2016). It is well known that smaller nozzles in flow focusing or electrospray geometry lead to tinier jets. However, miniaturization also reduces the robustness of such systems (e.g. increasing the likelihood of clogging). Thus, it is desirable to work at optimum conditions for both maximum speed v_j and minimum diameter D_j given a certain nozzle size. This entails the maximization of the driving pressure ΔP and the minimization of the liquid flow rate Q_ℓ for a steady operation, as can be noted from the established scaling laws for capillary cone-jets as a function of the flow properties and governing parameters: surface tension σ, viscosity μ_ℓ, density ρ_ℓ, electrical conductivity K, permittivity ε, and gas pressure ΔP_g or electrical pressure ΔP_{ES}. According to these laws, the jet speed and diameter scale as $v_j \approx (2\Delta P/\rho_\ell)^{1/2}$ and $D_j \approx (8\rho_\ell Q_\ell^2/\pi^2\Delta P)^{1/4}$, respectively. In

these laws, the driving pressure ΔP is given by either $\Delta P_{FF} \sim \Delta P_g$ for flow focusing or $\Delta P_{ES} \sim (\sigma^2 K^2 \rho_\ell / \varepsilon_o^2)^{1/3}$ for electrospray under the dominance of inertia and electrostatic suction (Gañán-Calvo & Montanero, 2009). Any accurate modeling of the jet behavior must contend with instability mechanisms within the fluid domain that may prevent the ideal steady jetting, which imposes some additional constraints to the problem. For a given Weber number We_ℓ^*, that should be within the range $1 \lesssim We_\ell = \rho_\ell v_j^2 D_j / 2\sigma \lesssim 20$, the maximum jet speed and the minimum jet diameter (or minimum liquid flow rate $Q_{\ell min}$) are limited by these restrictions. Since the liquid formulation fixes ΔP_{ES} in electrospray, which fixes the maximum jet speed, we can transform the optimization problem into that of finding the minimum possible flow rate for the dripping-jetting transition which has been explored in the previous chapter for flow focused jets and in the literature for pure electrospray jets (Ponce-Torres, 2018).

Chapter 5

Conclusion and prospects

> It is better to leave a vessel unfilled, than to attempt to carry it when it is full. If you keep feeling a point that has been sharpened, the point cannot long preserve its sharpness. When gold and jade fill the hall, their possessor cannot keep them safe. When wealth and honors lead to arrogance, this brings its evil on itself. When the work is done, and one's name is becoming distinguished, to withdraw into obscurity is the way of Heaven.
>
> Lao Tse

Once the work is done, it is time for reflections. This Ph. D. thesis has a clear devotion of being useful for a real purpose: theoretical, numerical and experimental studies for providing insight suitable for SFX and SMI.

In the first chapter we provide the reader a general introduction to the main aspects of steady liquid jets produced by either electrospray or flow

focusing. Likewise, the main challenges of sample delivery at SFX and SMI are properly addressed with a comprehensive review of the literature in the applied field.

In the Chapter 2, we focused on one of those challenges, the concept of a delivery method for a XFEL-drop synchronization of their respective frequencies of generation. Acoustic methods have been used so far for that purpose. Here, we did overcome the limitations of acoustic methods by operating the flow focusing configuration in the monosized dripping mode, which is properly identified and analyzed here for first time. We did derive the scaling law that govern the drop diameter as a function of the surface tension, the gaseous pressure and the feeding capillary diameter. So, the liquid flow rate does not affect the drop diameter at the first order. Consequently, a variation of the liquid flow rate only entails a change in the frequency of the droplet generation. This is a significant difference between this monosized dripping mode and the steady jetting mode, where both gas pressure and liquid flow rates turn out coupled for the jet diameter and frequency. An important question to be noted is the type of XFEL facilities that eventually could use this mode of flow focusing. Making some calculations based on our scaling laws, we can find $f = 7.124 \cdot 10^5 Q_\ell / D_d^3$, f in (Hz), Q_ℓ in (μL/min) and D_d in μm. For instance, a certain droplet diameter desired for an experiment $D_d \sim 40$ μm, we could vary the liquid flow rate Q_ℓ from 5 to 50 μL/min in a compatible way. So, the frequency of droplet generation would range from 55.7 to 556.6 Hz. Obviously, these hydrodynamic frequencies only could be synchronized with XFEL facilities with low repetition rates such as SwissFEL (100 Hz), SACLA (60 Hz), PAL-XFEL (60 Hz) and LCLS (120 Hz) offers. Additionally, the slow frequency between bunch packets in European XFEL could alternatively be used, reaching 10 Hz.

In the Chapter 3, we studied the capabilities of flow focusing at providing fast enough steady liquid jets for megahertz SFX experiments. We approached the problem through a theoretical analysis of the dripping jetting transition and its link to the global stability and the short-term response of the jet. The base flows and the corresponding linear global modes have been calculated from the Navier-Stokes equations to determine the asymptotic stability of those flows. The analysis has been conducted for wide ranges of the liquid viscosity and gas speed (applied pressure drop), and for a geometry similar to that considered in the experiments (Acero et

al., 2012). The flow rates corresponding to marginal stability agree reasonably well with the experimental values leading to dripping for large enough applied pressure drops. On the contrary, these theoretical predictions do not follow the experimental trend for small pressure drops (Weber numbers around and less than unity). To explain this pancy, the evolution of small perturbations introduced into the liquid meniscus has been studied by integrating over time the hydrodynamic equations for small gas speeds. We have found that those perturbations can grow while convected by the jet, pinching the free surface next to the discharge orifice. We conclude that the jetting-to-dripping transition is caused by asymptotic global instability for large applied pressure drops, and by the system's short-term response to perturbations for small values of this parameter. In the last part of the chapter, we commented the main insights from the use of flow focusing at MHz XFEL experiments, where we were fortunate to participate in collaboration with Henry N. Chapman's group. It is shown how the miniaturization of flow focusing can generate fast enough liquid jets for fulfilling with the constraints imposed by gap dynamics produced by the XFEL-liquid interaction at 1.1 MHz of XFEL repetition rate.

Lastly, in the Chapter 4 we did optimize the delivery of steady liquid jets by using both electrohydrodynamic fields and the assistance of gaseous boundary layers. We realized a comprehensive study about the limitations for the maximization and minimization of the jet diameter and jet speed, respectively. Indeed, we did introduce a novel method, *AEJ*, for its potential use at SMI experiments. Furthermore, we derived global scaling laws that govern the inherent relation between both cone-jet features at those extreme conditions. Also, we introduced the double AEJ version for delivering the sample through two coaxially delivered miscible liquid jets. This concept has the potential to deliver samples through steady liquid jets with diameters ranging from approximately 50 nm to around 1 μm. The lower limit would compatible with desirable conditions for Single-Molecule-Imaging (SMI), where a weakly enough backscattering is a prerequisite for detecting weak signals. Besides the tiny jets, their speed would considerably exceed the 100 m/s, which is interestingly compatible with XFEL experiments at megahertz repetition rates.

References

Acero, A. J., Ferrera, C., Montanero, J. M., & Gañán-Calvo, A. M. (2012). Focusing liquid microjets with nozzles. *J. Micromech. Microeng.*, *22*, 065011.

Anna, S. L., Bontoux, N., & Stone, H. A. (2003). Formation of dispersions using flow focusing in microchannels. *Appl. Phys. Lett.*, *82*, 364-366.

Berry, J. D., Davidson, M. R., & Harvie, D. J. E. (2013). A multiphase electrokinetic flow model for electrolytes with liquid/liquid interfaces. *Journal of Comp. Phys.*, *251*, 209-222.

Beyerlein *et al.*, K. R. (2015). Ceramic micro-injection molded nozzles for serial femtosecond crystallography sample delivery. *Review of Scientific Instruments*, *86*, 125104.

Bohne *et al.*, S. (2019). 3d printed nozzles on a silicon fluidic chip. *Review of Scientific Instruments*, *90*, 035108.

Boutet, S., Lomb, L., Williams, G. J., Barends, T. R. M., Aquila, A., Doak, R. B., ... Schlichting, I. (2012). High-resolution protein structure determination by serial femtosecond crystallography. *Science*, *337*(6092), 362–364. Retrieved from `http://science.sciencemag.org/content/337/6092/362` doi: 10.1126/science.1217737

Chapman *et al.*, H. N. (2011). Femtosecond x-ray protein nanocrystallography. *Nature*, *470*, 73-79.

Cherezov *et al.*, V. (2007). High-resolution crystal structure of an engineered human 2-adrenergic g protein coupled receptor. *Science*, *318*, 1258.

Chomaz, J. (2005). Global instabilities in spatially developing flows. *Annu. Rev. Fluid Mech.*, *37*, 357-392.

Cloupeau, M., & Prunet-Foch, B. (1994). Electrohydrodynamic spraying

functioning modes: A critical review. *J. Aerosol Sci.*, *25*, 1021-1036.

Cohen, I., Li, H., Hougland, J. L., Mrksich, M., & Nagel, S. R. (2001). Using selective withdrawal to coat microparticles. *Science*, *292*, 265-267.

Collins, R. T., Sambath, K., Harris, M. T., & Basaran, O. A. (2013). Universal scaling laws for the disintegration of electrified drops. *PNAS*, *110*, 4905-4910.

de Luca, L. (1999). Experimental investigation of the global instability of plane sheet flows. *J. Fluid Mech.*, *399*, 355-376.

de Luca, L., Costa, M., & Caramiello, C. (2002). Energy growth of initial perturbations in two-dimensional gravitational jets. *Phys. Fluids*, *14*, 289-299.

DePonte, D. P., Weierstall, U., Schmidt, K., Warner, J., Starodub, D., Spence, J. C. H., & Doak, R. B. (2008). Gas dynamic virtual nozzle for generation of microscopic droplet streams. *J. Phys. D: Appl. Phys.*, *41*, 195505.

Dizes, S. L. (1997). Global modes in falling capillary jets. *Eur. J. Mech. B/Fluids*, *16*, 761-778.

Eggers, J., & Villermaux, E. (2008). Physics of liquid jets. *Rep. Prog. Phys.*, *71*, 036601.

Fenn, J. B., Mann, M., Meng, C. K., Wong, S. F., & Whitehouse, C. M. (1989). Electrospray ionization for mass spectrometry of large biomolecules. *Science*, *246*, 64-71.

Forbes, T. P., & Sisco, E. (2014). Chemical imaging of artificial fingerprints by desorption electro-flow focusing ionization mass spectrometry. *Analyst*, *139*, 2982.

Gañán-Calvo *et al.*, A. M. (2018). Review on the physics of electrospray: From electrokinetics to the operating conditions of single and coaxial taylor cone-jets, and ac electrospray. *J. Aerosol Sci.*, *125*, 32-56.

Gañán-Calvo, A. M., López-Herrera, J. M., noz, N. R.-M., & Montanero, J. M. (2016). The onset of electrospray: the universal scaling law of the first ejection. *Scientific Reports*, *6*, 32357.

Gañán-Calvo, A. M. (1997). Cone-jet analytical extension of Taylor's electrostatic solution and the asymptotic universal scaling laws in electrospraying. *Phys. Rev. Lett.*, *79*, 217-220.

Gañán-Calvo, A. M. (1998). Generation of steady liquid microthreads

and micron-sized monodisperse sprays in gas streams. *Phys. Rev. Lett.*, *80*, 285-288.

Gañán-Calvo, A. M. (2004a). On the general scaling theory for electrospraying. *J. Fluid Mech.*, *507*, 203-212.

Gañán-Calvo, A. M. (2004b). Perfectly monodisperse microbubbling by capillary flow focusing: An alternate physical description and universal scaling. *Phys. Rev. E*, *69*, 027301.

Gañán-Calvo, A. M. (2005). Enhanced liquid atomization: From flow-focusing to flow-blurring. *Appl. Phys. Lett.*, *86*, 214101.

Gañán-Calvo, A. M. (2007). Electro-flow focusing: The high-conductivity low-viscosity limit. *Phys. Rev. Lett.*, *98*, 134503.

Gañán-Calvo, A. M., Ferrera, C., & Montanero, J. M. (2011). Universal size and shape of viscous capillary jets: application to gas-focused microjets. *J. Fluid Mech.*, *670*, 427-438.

Gañán-Calvo, A. M., González-Prieto, R., Riesco-Chueca, P., Herrada, M. A., & Flores-Mosquera, M. (2007). Focusing capillary jets close to the continuum limit. *Nature Phys.*, *3*, 737-742.

Gañán-Calvo, A. M., & Gordillo, J. M. (2001). Perfectly monodisperse microbubbling by capillary flow focusing. *Phys. Rev. Lett.*, *87*, 274501.

Gañán-Calvo, A. M., Lasheras, J. C., Dávila, J., & Barrero, A. (1994). The electrostatic spray emitted from an electrified conical meniscus. *J. Aerosol Sci.*, *25*, 1121-1142.

Gañán-Calvo, A. M., & Montanero, J. M. (2009). Revision of capillary cone-jet physics: Electrospray and flow focusing. *Phys. Rev. E*, *79*, 066305.

Gañán-Calvo, A. M., Montanero, J. M., Martín-Banderas, L., & Flores-Mosquera, M. (2013). Building functional materials for health care and pharmacy from microfluidic principles and Flow Focusing. *Adv. Drug Delivery Rev.*, *65*, 1447-1469.

García, F., & González, H. (2008). Normal-mode linear analysis and initial conditions of capillary jets. *J. Fluid Mech.*, *602*, 81-17.

González, H., & García, F. (2009). The measurement of growth rates in capillary jets. *J. Fluid Mech.*, *619*, 179-212.

Gordillo, J. M., Sevilla, A., & Campo-Cortés, F. (2014). Global stability of stretched jets: conditions for the generation of monodisperse micro-emulsions using coflows. *J. Fluid Mech.*, *738*, 335-357.

Herrada, M. A., López-Herrera, J. M., Gañán-Calvo, A. M., Vega, E. J., Montanero, J. M., & Popinet, S. (2012). Numerical simulation of electrospray in the cone-jet mode. *Phys. Rev. E*, *86*, 026305.

Herrada, M. A., & Montanero, J. M. (2016). A numerical method to study the dynamics of capillary fluid systems. *J. Comput. Phys.*, *306*, 137-147.

Huerre, P., & Monkewitz, P. A. (1990). Local and global instabilites in spatially developing flows. *Annu. Rev. Fluid Mech.*, *22*, 473-537.

Jaworek, A. (2007). Electrospray droplet sources for thin film deposition. *J. Mater. Sci.*, *42*, 266-297.

Korczyk *et al.*, P. M. (2011). Effects of unsteadiness of the rates of flow on the dynamics of formation of droplets in microfluidic systems. *Lab on a Chip*, *11*, 173-175.

Leib, S. J., & Goldstein, M. E. (1986a). Convective and absolute instability of a viscous liquid jet. *Phys. Fluids*, *29*, 952-954.

Leib, S. J., & Goldstein, M. E. (1986b). The generation of a capillary instability on a liquid jet. *J. Fluid Mech.*, *168*, 479-500.

López-Herrera, J. M., Gañán-Calvo, A., Popinet, S., & Herrada, M. A. (2015). Electrokinetic effects in the breakup of electrified jets: A Volume-Of-Fluid numerical study. *Int. J. Multiphase Flow*, *71*, 14-21.

López-Herrera, J. M., Popinet, S., & Herrada, M. A. (2011). A charge-conservative approach for simulating electrohydrodynamic two-phase flows using volume-of-fluid. *J. Comput. Phys.*, *230*, 1939-1955.

Loscertales, I. G., Barrero, A., Guerrero, I., Cortijo, R., Marquez, M., & Gañán-Calvo, A. M. (2002). Micro/nano encapsulation via electrified coaxial liquid jets. *Science*, *295*, 1695-1698.

Mcneil, B. W. J., & Thompson, N. R. (2010). X-ray free-electron lasers. *Nature Photonics*, *4*, 814-821.

Montanero, J. M., Rebollo-Muñoz, N., Herrada, M. A., & Gañán-Calvo, A. M. (2011). Global stability of the focusing effect of fluid jet flows. *Phys. Rev. E*, *83*, 036309.

Nelson *et al.*, G. (2016a). Three-dimensional-printed gas dynamic virtual nozzles for x-ray laser sample delivery. *Optics Express*, *24*, 11515-11530.

Nelson *et al.*, G. (2016b). Three-dimensional-printed gas dynamic virtual

nozzles for x-ray laser sample delivery. *Opt. Express*, *24*, 11515-30.

Neutze, R., Wouts, R., Spoel, D. V. D., Weckert, E., & Hajdu, J. (2000). Potential for biomolecular imaging with femtosecond x-ray pulses. *Nature*, *406*, 752-757.

Oberthür *et al.*, D. (2017). Double-flow focused liquid injector for efficient serial femtosecond crystallography. *Scientific Reports*, *7*, 44628.

Pebay-Peyroula, E. (1997). X-ray structure of bacteriorhodopsin at 2.5 angstroms from microcrystals grown in lipidic cubic phases. *Science*, *277*, 1676–1681.

Pellegrini, C., Marinelli, A., & Reiche, S. (2016). The physics of x-ray free-electron lasers. *Rev. Mod. Phys.*, *88*, 102601.

Pellegrini *et al.*, C. (2016). The physics of x-ray free-electron lasers. *Rev. Mod. Phys.*, *88*, 015006.

Pillai, R., Berry, J. D., Harvie, D. J. E., & Davidson, M. R. (2016). Electrokinetics of isolated electrified drops. *Soft Matter*, *12*, 3310-3325.

Rayleigh, J. W. S. (1892). On the instability of a cylinder of viscous liquid under capillary force. *Phil. Mag.*, *35*, 145-155.

Rayleigh, L. (1882). Xx. on the equilibrium of liquid conducting masses charged with electricity. *Philosophical Magazine Series 5*, *14*(87), 184-186. Retrieved from `http://dx.doi.org/10.1080/14786448208628425` doi: 10.1080/14786448208628425

Roessler *et al.*, C. G. (2016). Acoustic injectors for drop-on-demand serial femtosecond crystallography. *Structure*, *24*, 631-640.

Rubio-Rubio, M., Sevilla, A., & Gordillo, J. M. (2013). On the thinnest steady threads obtained by gravitational stretching of capillary jets. *J. Fluid Mech.*, *729*, 471-483.

Sauter, U. S., & Buggisch, H. W. (2005). Stability of initially slow viscous jets driven by gravity. *J. Fluid Mech.*, *533*, 237-257.

Saville, D. A. (1997). Electrohydrodynamics: The Taylor-Melcher leaky dielectric model. *Annu. Rev. Fluid Mech.*, *29*, 27-64.

Schmid, P. J. (2007). Nonmodal stability theory. *Annu. Rev. Fluid Mech.*, *39*, 129-162.

Seibert *et al.*, M. M. (2011). Single mimivirus particles intercepted and imaged with an x-ray laser. *Nature*, *470*, 78-82.

Si, T., Feng, H., Luo, X., & Xu, R. X. (2014). Formation of steady

compound cone-jet modes and multilayered droplets in a tri-axial capillary flow focusing device. *Microfluid Nanofluid*, *1*, 1-11.

Si, T., Li, F., Yin, X.-Y., & Yin, X.-Z. (2009). Modes in flow focusing and instability of coaxial liquid-gas jets. *J. Fluid Mech.*, *629*, 1-23.

Sierra *et al.*, R. (2012). Nanoflow electrospinning serial femtosecond crystallography. *Acta Crystallographica Section D: Biological Crystallography*, *68*, 1584-1587.

Sierra *et al.*, R. (2015). Concentric-flow electrokinetic injector enables serial crystallography of ribosome and photosystem ii. *Nature Methods*, *13*, 59-62.

Stan *et al.*, C. A. (2016). Liquid explosions induced by x-ray laser pulses. *Nature Physics*, *12*, 966-971.

Takáts, Z., Wiseman, J. M., Gologan, B., & Cooks, R. G. (2004). Mass spectrometry sampling under ambient conditions with desorption electrospray ionization. *Science*, *306*, 471-473.

Tammisola, O., Lundell, F., & Soderberg, L. D. (2011). Effect of surface tension on global modes of confined wake flows. *Phys. Fluids*, *23*, 014108.

Tammisola *et al.*, O. (2011). Stabilizing effec of surrounding gas flow on a plane liquid sheet. *J. Fluid Mech*, *672*, 532.

Tammisola *et al.*, O. (2012). Surface tension-induced global instability of planar jets and wakes. j. fluid mech. *J. Fluid Mech.*, *713*, 632-658.

Taylor, G. (1964). Disintegration of water drops in electric field. *Proc. R. Soc. Lond. A*, *280*, 383-397.

Taylor, G. I. (1950a). The formation of a blast wave by a very intense explosion. ii. the atomic explosion of 1945. *Proceedings of the Royal Society of London. Series A, Mathematical and Physical Sciences.*, *201*, 175-186.

Taylor, G. I. (1950b). The formation of a blast wave by a very intense explosion. i. theoretical discussion. *Proceedings of the Royal Society of London. Series A, Mathematical and Physical Sciences.*, *201*, 159-174.

Theofilis, V. (2011). Global linear instability. *Annu. Rev. Fluid Mech.*, *43*, 319-352.

Trebbin, M., Kruger, K., DePonte, D., Roth, S. V., Chapman, H. N., & Forster, S. (2014). Microfluidic liquid jet system with compatibility for atmospheric and high-vacuum conditions. *Lab on a Chip*, *14*,

1733-1745.

Utada, A. S., Lorenceau, E., Link, D. R., Kaplan, P. D., Stone, H. A., & Weitz, D. A. (2005). Monodisperse double emulsions generated from a microcapillary device. *Science*, *308*, 537-541.

Vega, E. J., Montanero, J. M., Herrada, M. A., & Gañán-Calvo, A. M. (2010). Global and local instability of flow focusing: The influence of the geometry. *Phys. Fluids*, *22*, 064105.

Vonnegut, B., & Neubauer, R. L. (1952). Production of monodisperse liquid particles by electrical atomization. *Journal of Colloid Science*, *7*(6), 616 - 622.

Weierstall *et al.*, U. (2014). Lipidic cubic phase injector facilitates membrane protein serial femtosecond crystallography. *Nature communications*, *5*, 3309.

White *et al.*, T. A. (2012). Crystfel: a software suite for snapshot serial crystallography. *J. Appl. Cryst.*, *45*, 335-341.

White *et al.*, T. A. (2016). Recent developments in crystfel. *J. Appl. Cryst.*, *49*, 680-689.

Wiedorn *et al.*, M. O. (2018). Megahertz serial crystallography. *Nature Communications*, *9*, 4025.

Yakubenko, P. A. (1997). Global capillary instability of an inclined jet. *J. Fluid Mech.*, *346*, 181-200.

Zeleny, J. (1914). The electrical discharge from liquid points, and a hydrostatic method of measuring the electric intensity at their surfaces. *Phys. Rev.*, *3*, 69-91.

Zeleny, J. (1917). Instability of electrified liquid surfaces. *Phys. Rev.*, *10*, 1-6.